UNIVERSITY OF NOVA GORICA
SCHOOL OF SCIENCE

STUDY OF ELECTRONIC STATES OF THIN METAL FILMS ON HEAVY METAL SURFACES

MASTER'S THESIS

Luka Novinec

Mentor: prof. dr. Sandra Gardonio
Mentor: dr. Paolo Moras

Nova Gorica, 2018

UNIVERZA V NOVI GORICI
FAKULTETA ZA NARAVOSLOVJE

ŠTUDIJ ELEKTRONSKIH STANJ V TANKIH, KOVINSKIH FILMIH NA POVRŠINAH TEŽKIH KOVIN

MAGISTRSKA NALOGA

Luka Novinec

Mentor: prof. dr. Sandra Gardonio
Mentor: dr. Paolo Moras

Nova Gorica, 2018

Acknowledgement

After my bachelor thesis I decided to continue the collaboration with the people who gave me a lot of knowledge and support through my studies. I acknowledge researchers from VUV-Photoemission and BaDElPh beamlines at Elettra Synchrotron Laboratory, Dr. Paolo Moras, Dr. Polina Sheverdyaeva and Dr. Luca Petaccia for their support and supervision during experiments while being on Erasmus Training program at Elettra-Sincrotrone Trieste. I thank Dr. Mario Italo Trioni (ISTM-CNR Milano), Dr. Stefano Iacobucci (ISM-CNR Rome), Dr. Francesco Offi (ISM-CNR Rome) and Dr. Serguei Gorovigov (Canadian Light Source) for the courtesy of sharing their calculated band structures and some preliminary angle resolved photoemission spectroscopy (ARPES) data of Yb on Mo(110).

And last but not least I thank my family and friends for believing in me.

Abstract

The focus of this thesis is the preparation and characterisation of metal/heavy metal heterostructures. Two ferromagnetic metals, Fe and Gd, and a divalent rare earth metal, Yb, have been selected to form thin films on W(110) and Mo(110) substrates. The conditions for atomically uniform film growth were successfully established in the case of Fe on W(110) and Mo(110) and in the case of Yb on Mo(110). Quantum well states were observed by means of angle resolved photoemission in Fe and Yb films on Mo and W substrates. All the experimental work has been performed at VUV-Photoemission (ISM-CNR) and BaDElPh beamlines at Elettra-Sincrotrone Trieste.

Povzetek

V magistrskem delu smo se osredotočili na pripravo in karakterizacijo heterogenih večplastnih tankih filmov sestavljenih iz kovin ter težkih kovin. Za izdelavo vzorcev smo izbrali dve feromagnetni kovini, Fe in Gd, ter eno divalentno kovino iz redkih zemelj, Yb. Tanke filme smo nanašali na kristalno površino volframa W(110) ter molibdena Mo(110). V primeru Fe na površini W(110) in Mo(110) ter Yb na povšini Mo(110) smo uspešno določili pogoje, potrebne za nanašanje atomsko enakomernih filmov. S pomočjo kotno odvisne fotoemisije smo preučevali kvantna stanja v Fe in Yb filmih na Mo in W kristalih. Celotno eksperimentalno delo je potekalo na žarkovnih linijah VUV-Photoemission inštituta (ISM-CNR) ter BaDElPh pri sinhrotronu Elettra v Trstu.

Contents

List of Figures

1 Introduction

The scope of the thesis is the preparation of atomically flat and thin metallic films grown on heavy metal (HM) surfaces with the final objective of observing quantum well states (QWSs). The investigated heterostructures are Fe, Gd and Yb deposited on Mo(110) and W(110).

From the technological point of view, the electronic and the magnetic properties of thin films have been exploited in the field of Spintronics. Spintronics is a new paradigm for electronics which utilizes the electron's spin in addition to its charge for device functionality. Up to date the biggest commercial impact of spintronics has been in the area of spin valves used in magnetic hard disk drives. Spin valves are based on giant magnetoresistive (GMR) effect where two ferromagnetic layers sandwich a non-ferromagnetic metal spacer of nanometer thickness. The resistivity in metal spacer depends on the magnetization orientation of two ferromagnetic layers. By manipulating the magnetization orientation (parallel or anti-parallel) the valve can be in "open" (low resistance) or "close" (high resistance) state, respectively. The integration of these tri-layer structures in hard disk drives has increased enormously the areal storage density. With GMR the electrical read out memory elements improved but the magnetic writing remains the object of major research efforts [1]. Materials with stable magnetization, which are attractive for data storage, usually have large coercivity and perpendicular magnetic anisotropy [2] and are hard to write [3]. Local electric fields [4] [5] and currents [6] [7] [8] can be used to reverse the polarity of nano-sized magnets. Despite these findings, simple reversal of a high-coercivity single layer ferromagnet remains a challenge.

Field-induced magnetization switching is known to be a size and power consuming technique [9] and different mechanisms, like spin transfer torque (STT), are investigated as an alternative. STT arise whenever the flow of spin-angular momentum through a sample is not constant, but has sources or leaks. This can happen, for example, in a structure like the one reported in Fig. 1.1. An unpolarized current is spin polarized by a magnetic thin layer ("Ferro 1"), and subsequently altered by a second magnetic layer ("Ferro 2") that possess a magnetization non collinear with the layer "Ferro 1". During this process the layer "Ferro 2" will necessarily adsorb part of the spin-angular momentum of the current. A large current can in principle generate a force big enough to shift the magnetization direction of the "Ferro 2" layer. The mechanism described here can be used to develop magnetic tunnel junction which utilize STT to switch reversibly the magnetization in one of the layers.

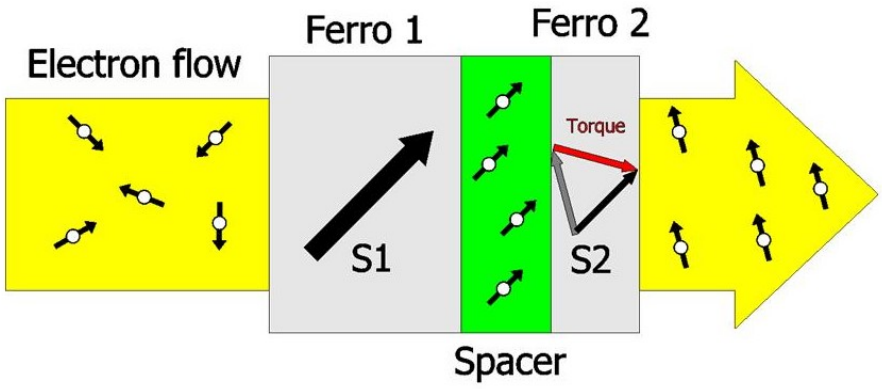

Figure 1.1: Schematic illustration of STT. By passing through a ferromagnetic thick layer, the flow of electrons becomes polarised by torque exerted on spin vectors. As a result, all moments are aligned and point in the same direction. In the second ferromagnet effect is similar, except that here a portion of spin-angular momentum is absorbed by the magnetic thin film and gives rise to reorientation of its magnetization orientation [7].

The spin orbit torque (SOT) is attracting the attention since it allows to control the magnetization at bi-layer systems made of thin ferromagnetic layers (FM) on heavy metals (HM), like Pt and Ta [10] [11]. The origin of observed SOT in FM/HM heterostructures is related to the spin-orbit coupling and can be due to different effects: Spin Hall effect, which produces a pure spin current when the charge current passes through the HM layer and exerts a torque on the magnetization or because of the interfacial Rashba effect that causes an accumulation of spins at the interface which force the moments to change their direction by direct exchange coupling. Based on the literature, none of the mentioned effects exhaustively explains the observed SOT at the FM/HM heterostructures. One of the reasons is that the FM and HM layers can affect the electronic structure of each other at the interface which in turn can change the spin-orbit coupling. In this context, it is extremely important to gain knowledge about the electronic structure of FM/HM heterostructures.

Angle resolved photoemission is the leading spectroscopy tool to access the electronic structure of materials. However, it allows to probe electrons only within few Åbelow the surface of a material. The extreme surface sensitivity of this technique does not allow to access directly the electronic structure of buried layers and interfaces in heterostructures. One strategy to overcome this problem is to exploit electron interference effects occurring in atomically uniform layers deposited on the surface of a single crystal [12, 13].

When the layer is smooth and its thickness is of the order of few nanometers, electrons form discrete QWSs i.e. states confined between the surface layer and the substrate, in analogy to the textbook particle in a box picture [14]. QWSs appear as discrete peaks in ARPES spectra [15]. Experimental results taken from Ag films grown on Si(001) are shown in Fig. 1.3 [16]. The discrete peaks in the spectra correspond to QWSs, or standing waves of electrons formed by coherent multiple reflections between the two

boundaries of the film: the substrate and the vacuum (see Fig. 1.2).

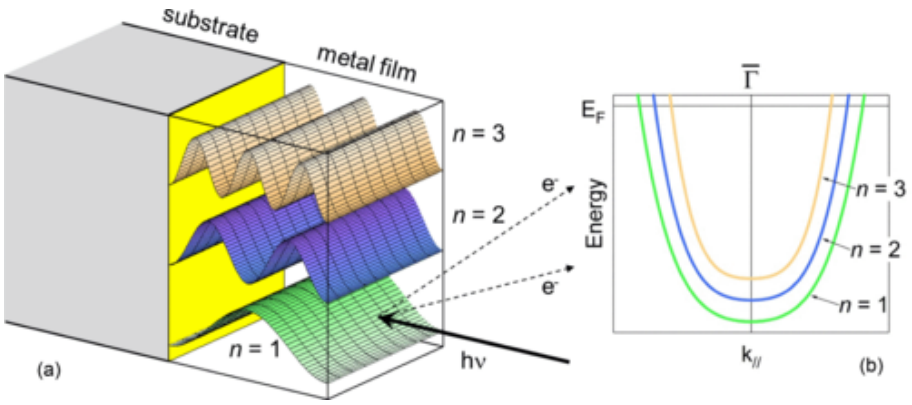

Figure 1.2: (a) Surface (transparent) and interface (yellow) planes act as potential walls for the film valence electrons. The confined geometry gives rise to a set of two-dimensional standing waves, called QW states, that extend in the whole film thickness. These states can be labeled with the main quantum number n, i.e., the number of maxima of the respective charge densities along the direction of confinement. (b) The extended spatial character of the QW-state wave functions makes their energy-momentum band dispersion, observable by angle-resolved photoemission spectroscopy, an indirect probe of interface interactions [17].

The energies of the QWSs are determined by the Bohr-Sommerfeld quantization rule [15]:

$$2kNt + \Phi = 2n\pi \tag{1.1}$$

where k is the magnitude of the wave vector of the Bloch electron along the surface normal direction, t is the mono-layer thickness, N the number of mono-layers, Φ is the sum of the phase shifts at the two film boundaries, and n is the main quantum number.

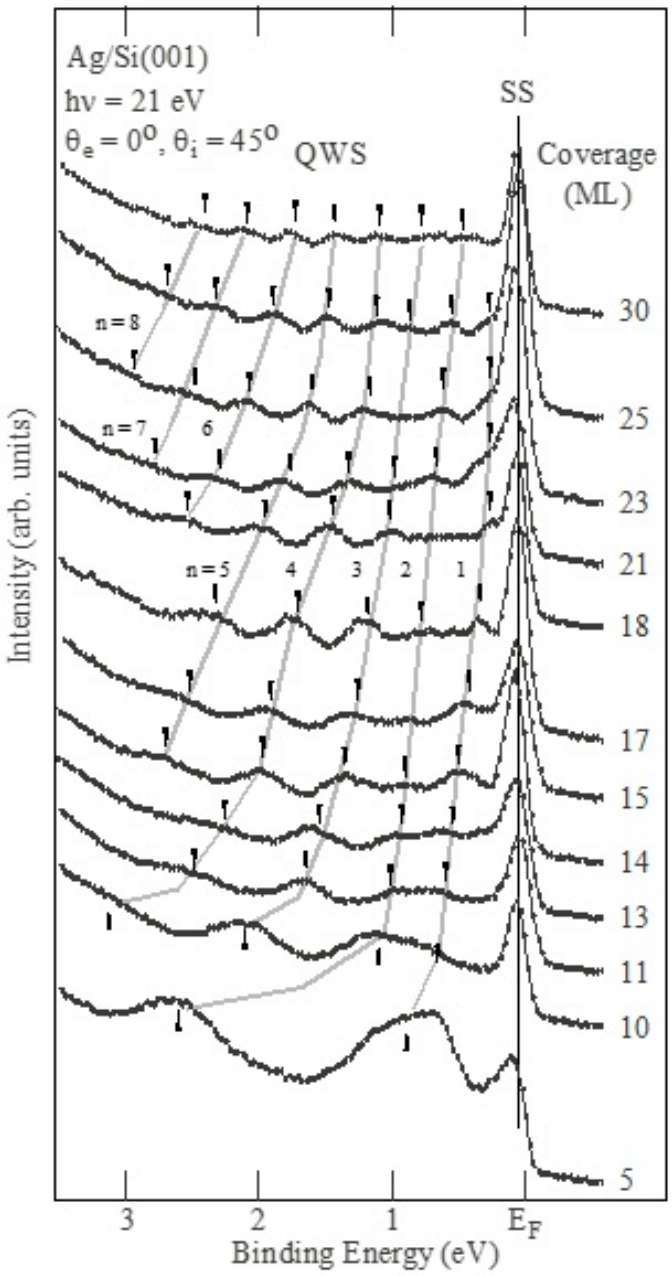

Figure 1.3: Angle resolved photoemission spectra measured on film of Ag, grown on Si(001) surface, having different thicknesses. The spectra are measured at normal emission ($k_{||}$=0). The peak positions of the corresponding energy levels (n=1, 2, 3, ...) are marked and connected with each other by grey lines [16].

As an example of QWSs detected by means of photoemission spectroscopy, the ARPES spectra measured on a film of Ag grown on Si (001) are reported in Fig. 1.3 [16]. The spectra, measured as a function of Ag thickness and at normal emission ($k_{||}$=0), present an intense surface state peak close to the Fermi energy (E_f) that does shift in energy as a function of the film thickness. The other peaks, at higher binding energy (BE), systematically change their BE as a function of the thickness as expected by the variation of the width of the potential well, i.e. the thickness of the Ag

films (Nt in the formula 1.1), where the valence electrons are confined. The different QWSs are labelled with quantum number n = 1-8 (see Fig. 1.3). Both the wave vector and the phase shift depend on energy (see Formula 1.1). By measuring the BE of QWSs as a function of the film thickness is possible to solve the equation 1.1 which in turn give the bulk band structure E(k) [15, 18].

An important requisite for observing QWSs is to produce a very smooth metal film. Like in the case of visible light for optical mirror, if the roughness of the film at the interface with the substrate and at its surface is of the order the electron wavelength of QWSs, the reflectivity at that barriers decreases and in the worst case the QWSs are completely quenched. In this sense, the sharpness of the QWSs observed with ARPES is a proof of film smoothness. Experimentally, the preparation of the material requires to grow layer by layer (or Frank van der Merwer) films or to form atomically flat thin films [19].

In the present thesis, devoted to the preparation and ARPES characterization of metal/HM heterostructures, we selected two ferromagnetic elementary metals, Fe and Gd, and a divalent rare earth metal, Yb, to form thin films on W(110) and Mo(110) substrates. W and Mo have been chosen because they are isoelectronic and have similar crystalline structure but different atomic number which enables us to understand if there is any contribution of the substrate, in terms of spin-orbit interaction, to the overlayer electronic structure. The spin-orbit interaction is higher in W than in Mo. The preparation and electronic structure characterization of Co films on Mo(110) and W(110) have been performed previously [17, 20]. Co films on W(110) present magnetic, i.e. exchange-split, QW states. The band dispersion of these states along equivalent crystallographic directions is asymmetric, in contrast with the expectation for centro-symmetric systems. The asymmetries can be reversed with respect to the centre of the Surface Brillouin zone by switching the in-plane magnetization of the Co films [17]. The results here obtained for Fe films on Mo(110) and on W(110) extend the knowledge on the QWSs behaviour to another 3d ferromagnetic material on HM substrates. Rare earth films on HM substrates, supporting QWSs, are poorly explored. To our knowledge, QWSs have been observed in the case of Gd on W(110) only for coverages up to 4 ML [21]. The objective here is to find the experimental condition for growing smooth film of Gd on W(110), with thickness higher than 4 ML, that possibly show electron confinement effects.

Yb has been chosen for its borderline electronic and magnetic properties which makes this metal still very interesting for both fundamental and applicative aspects. Unlike most of the rare-earth metals, Yb is divalent and has anomalous physical properties in comparison to other rare earth metals. Because of the complete filling of the 4f shell in Yb, it is expected that this metal is nonmagnetic. However, depending on the local atomic coordination and chemical environment, the valence of metals such as Yb can change and its electronic structure is not obvious. There is in fact experimental evidence for a finite $4f$ moment in the paramagnetic behaviour of β-phase Yb [22], indicating a small $4f^{13}$ admixture to the ground state.

Moreover, a new phase of Yb has been prepared by epitaxial growth at low temperatures having a fcc crystal structure such as β-Yb metal [23]. What is still not clear is whether this phase is characterized by an increased $4f$ hybridization with valence states or by a change in the $4f$-level position alone. In this context, the objective of this thesis is the preparation, in-situ, of flat Yb films on the Mo(110) surface in order to observe and characterize QWSs. As mentioned above, QWSs can be used to have better insight about the electronic band structure of metallic Yb, which in turn depends on the electronic configuration of Yb and its crystalline structure.

The experimental work here presented has been conducted at the VUV-Photoemission and BaDElPh beamlines at Elettra Synchrotron (Italy). The two ultra high vacuum (UHV) systems, where the samples were prepared and characterized, are described in Chapter 2 together with basics concepts related to the experiemental techniques used. The description of the preparation of films of on Mo(110) and on W(110), of Yb on Mo(110), and of Gd on W(110) is reported in Chapter 3. The characterization of the electronic properties, by means of ARPES, of Fe and Yb films are presented and discussed in Chapter 4. Conclusions and future prospectives are in Chapter 5.

2 Experiment

All the experiments presented in this thesis were carried out at the VUV-Photoemission and BaDElPh beamlines at Elettra (Trieste). Both beamlines are exploiting photoemission spectroscopy (PES) technique, using synchrotron radiation, for studying the electronic and chemical structure of solids. The experimental set ups available at both beamlines are equipped with conventional apparatus for the *in-situ* preparation and characterization of metal surfaces and thin films.

PES technique is based on photoelectric effect where incoming monochromatic UV or soft X-ray light of energy $h\nu$, excite electrons form occupied energy levels of the solid having binding energy E_B. In a typical PES experiment the intensity of the emitted electrons as a function of their kinetic energy E_{kin} and emission angle θ (Fig. 2.1) are measured. Electron energy analyser equipped with multi-channel detectors allow to measure 2D intensity maps $I(\theta, E_{kin})$ from which can be extracted energy distribution curves (EDCs) that correspond to photoemission intensity signal measured at a certain emission angle or momentum distribution curves (MDCs) obtained at certain E_{kin}. In the photoemission process, the electrons that do not experience inelastic scattering inside the solid and reach the surface with an energy sufficient to overcome the potential barrier ϕ at the interface surface/vacuum, escape the solid and conserve the energy and parallel momentum ($k_{||}$) [19]. For the electrons escaping the solid without inelastic scattering, the two equations:

$$E_B = h\nu - E_{kin} - \Phi \tag{2.1}$$

$$|k_{||}| = \frac{\sqrt{2mE_{kin}}}{\hbar}\sin\theta = 0.512\sqrt{E_{kin}}\sin\theta \tag{2.2}$$

are valid, and they are collected by the electron analyser and identified as peaks on photoemission spectra. While the other photoelectrons that encounter energy loss, will add to the background of the spectrum. In this way in the spectrum we can clearly identify features due to the electronic excitation from core levels and valence band states and the continuous background of inelastic secondary electrons. When both E_{kin} and θ are measured, the technique is called ARPES and this way the band structure of solid or of the film is measured. In this thesis, ARPES is used to acquire the 2D photomemission intensity maps (Fig. 2.1 (b)) and for performing Fermi surface mapping. In the first case, each electron collected by the electron spectrometer and reaching the 2D multi-channel, is identified by its E_{kin} and emission angle θ at constant azimuthal emission angle Φ (see Fig. 2.1). These data are automatically processed via software and 2D photoemission intensity maps are produced using the formulas (2.1) and (2.2) which give the relation between E_{kin}, E_B and $k_{||}$. In the case of Fermi surface mapping, in the experimental set ups used in this thesis, the Fermi surfaces have been

measured by rotating azimuthally the sample (Φ angle in Fig. 2.1) and scanning with the angular aperture of the analyser at different polar angle (θ angle in Fig. 2.1).

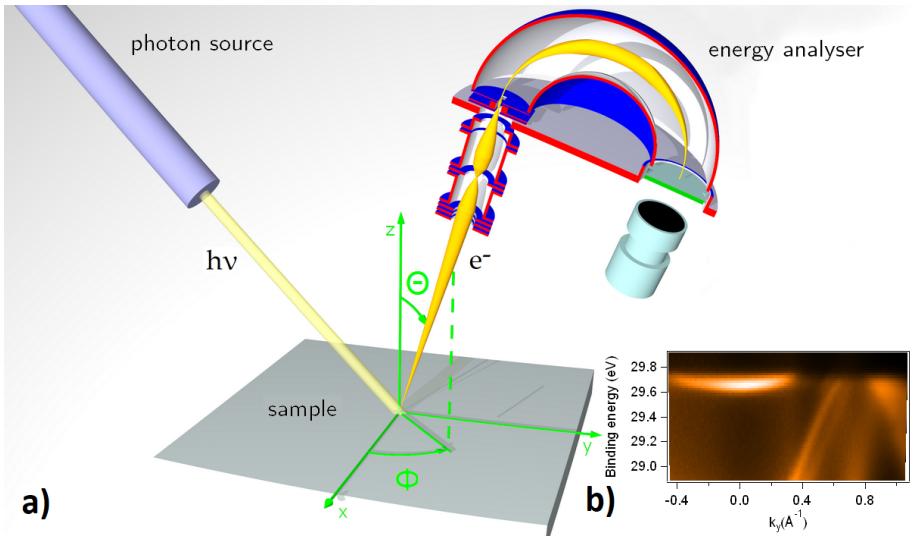

Figure 2.1: Schematic diagram of the experimental set up for photoemission experiments. (a) X-ray or UV light with a $h\nu$ energy illuminate the sample and excite the electrons from their occupied states. The emitted electrons are collected by the electron spectrometer as a function of their E_{kin} and polar emission angle θ and fixed (or variable) azimuthal emission angle Φ depending if 2D photoemission intensity maps or Fermi surfaces are measured. (b) An example of a 2D photoemission intensity map.

As can be seen in Fig. 2.2 (a), the shaded area is the scattering plane of photoelectrons that are collected at different polar angles θ by an electron spectrometer equipped with multi-channel plate detector. The axis of azimuthal rotation (Φ) is perpendicular to the sample surface, θ=0. At every step of rotation (angular steps of 1°) the photoemission data or constant energy cuts were acquired within $0° < \theta < —25°$ as a function of (Φ) (See Fig. 2.2 (b)). By using this technique asymmetries related to the light incidence angle that could arise in other Fermi surface ARPES geometries are avoided.

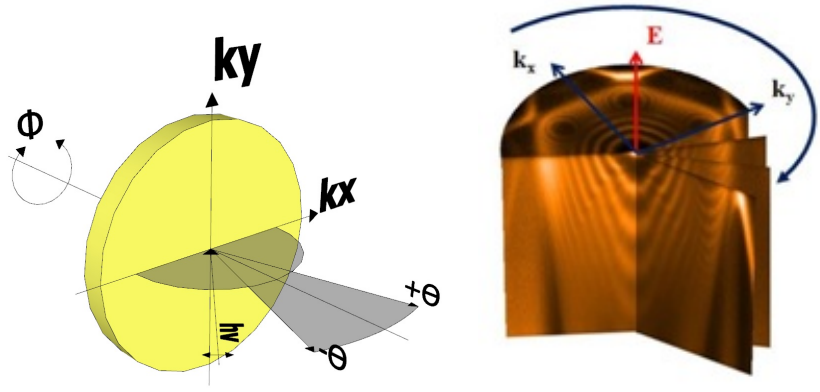

(a) (b)

Figure 2.2: (a) Schematic of experimental geometry for ARPES Fermi surface measurements with variable Φ azimuthal angle. (b) Reconstruction of constant energy cuts acquired as a function of Φ.

When only E_{kin} is analysed, the technique is known as angle-integrated PES. When the photon energy used is in the range of X-rays, the PES is called x-ray Photoemission Spectroscopy (XPS). Performing XPS allows to access deep core levels of solids and information about the surface chemical composition, concentration of the atomic species and chemical environment can be obtained [19]. XPS is used in this thesis during the preparation of surfaces and thin film with the scope of obtaining information of the cleanliness and an estimation of the film thickness.

Photoemission spectroscopy, being an electron spectroscopy technique, is a surface sensitive methodology that. In the favourable energy interval of 20 - 200 eV, the surface sensitivity is less than 10 Å[19]. This is undoubtedly a favourable property that makes PES the leading technique for obtaining information about the electronic/chemical structure of heterostructures, but because of that, it is required to prepare surfaces and thin films extremely clean and ordered. The ARPES and XPS measurements are therefore done in ultra-high vacuum environment (UHV) chambers and the surfaces are specially prepared before the measurements (see Chapter 3). With the exception of the XPS measurements of Gd on W(110), all the photoemission measurements reported in this thesis have been done using synchrotron light sources. Among the most significant properties of synchrotron radiation, the high intensity and tunable energy it produces, makes this source particularly effective in the study of the electronic properties of surfaces and thin films. Depending on the beamline characteristics, a variable range of photon energy can be selected and is possible to tune the ionization cross section and in this way gain information on specific valence band states or perform depth-dependent chemical analysis. Moreover, the higher photon intensity of a synchrotron, with respect to conventional UV or X-ray sources, results in shorter acquisition time. Fast acquisition is particularly important when examining materials such as transition metals and rare earths that are quickly contaminated.

Preparation and characterization of studied heterostructures Fe on Mo(110)

and W(110) (Paragraph 3.2 and 4.2, respectively) and Yb on Mo(110) (Paragraph 3.3 and 4.1, respectively) were performed at VUV-Photoemission beamline while Gd on W(110) (Paragraph 3.4) was studied at BaDElPh beamline at Elettra Sicrotrone Trieste.

VUV-Photoemission beamline [24] has been designed primarily for surface and solid state experiments involving high resolution photoemission with synchrotron radiation of 20 to 900 eV. With a photon flux that varies depending on the energy, from $1.4\text{x}10^{13}$ to $5\text{x}10^{10}$ photons/sec/0.1%bw/200mA in a spot of maximum size of 0.5 mm. The end station consists of three, valve separated UHV chambers and the schematic view is reported Fig 2.3. Samples are transferred from ambient to UHV by using the load lock chamber. This chamber is also equipped with a high temperature heating station where, by using electron bombardment, the samples can reach the temperatures of about 1700 K. In the same chamber are also available leak valves for inletting gases and sample treatments in gas atmosphere up to 10^{-2} mbar of oxygen. In the same chamber the films of Fe were uniformly and permanently magnetized by passing high-current pulses through a coil placed near the sample.

The preparation chamber has all necessary equipment for high quality sample preparation. The horizontal manipulator allows the sample temperature to vary from 100 K to 500 K. Surface cleaning can be done by using Ar+ sputtering technique while for film deposition one Omicron and three home-made exchangeable sources are mounted. An estimation of the evaporation rate, during the film deposition, can be done using a quartz microbalance. The samples surface crystalline structure is monitored by using low energy electron diffraction (LEED) optics. The base pressure in the chamber is $2\text{x}10^{-10}$ mbar.

Main chamber is hosting Scienta R4000-WAL electron analyser with variable acceptance angle (7-30 degrees). The analyser itself is mounted at 45° to the beam direction. During the measurements the sample is mounted on vertical manipulator with cooling possibility (9 K to 13 K) and motorized azimuthal angle motion that allows automatic acquiring of Fermi surfaces with angle step less than 0.01° for ±160°. The pressure in which the chamber operates is in 10^{-11} mbar regime.

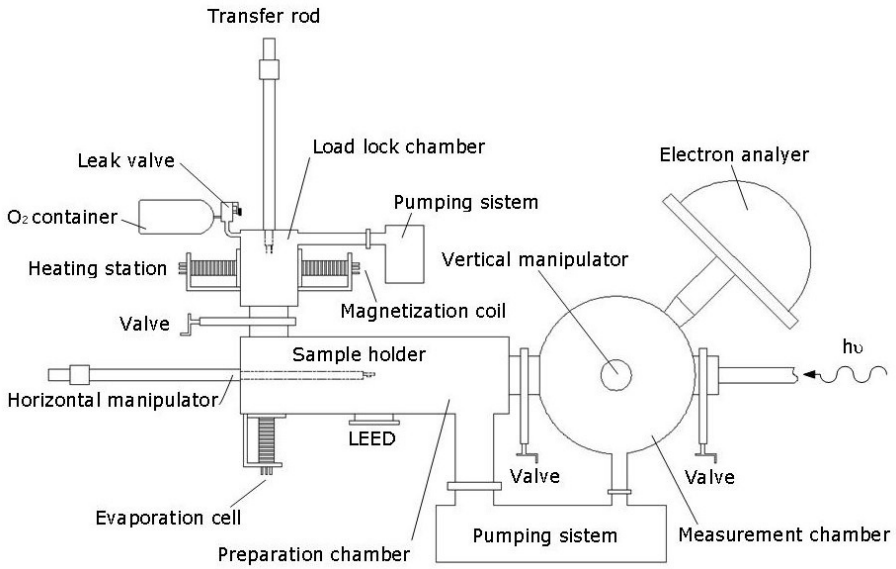

Figure 2.3: Schematic view of VUV-Photoemission beamline at Elettra Sincrotrone (Trieste). The experimental set-up consists of loadlock chamber (substrate cleaning), preparation chamber (sample preparation) and measurement chamber (ARPES measuremets). The whole system operates in UHV conditions and has transfer tools for *in-situ* sample preparation and studies.

BaDelPh beamline [25] is similar to VUV-Photoemission or any other photoemission beamline except in one crucial aspect. The photon energy of an incoming beam is 4.6 to 40 eV with high flux and high resolution. Because of this, low photon regime (5-10 eV) provides enhanced bulk sensitivity and allows for high momentum and energy resolution. This is what makes this beamline unique and interesting for the experiments devoted to energy and band mapping.

As can be seen in Fig. 2.4, also BaDElPh beamline has three UHV chambers separated by valves. The heater chamber is equipped with loadlock, 7-slot parking device and an electron bombardment heater stage for high temperatures (up to about 2400 K). The sample preparation is done in preparation chamber where ion sputter gun and different evaporators can be used for in-situ cleaning and thin film growth. The base pressure in both chambers is in the order of 10^{-10} mbar.

All the measurements are performed in analysis chamber where SPECS Phoibos 150 spherical analyser with a 2D-CCD detector system is installed. For various applications the chamber is equipped also with He UV lamp and Al&Mg X-ray sources, LEED optics, gas cell and a residual gas analyser (RGA) while the base pressure is in low 10^{-11} mbar region.

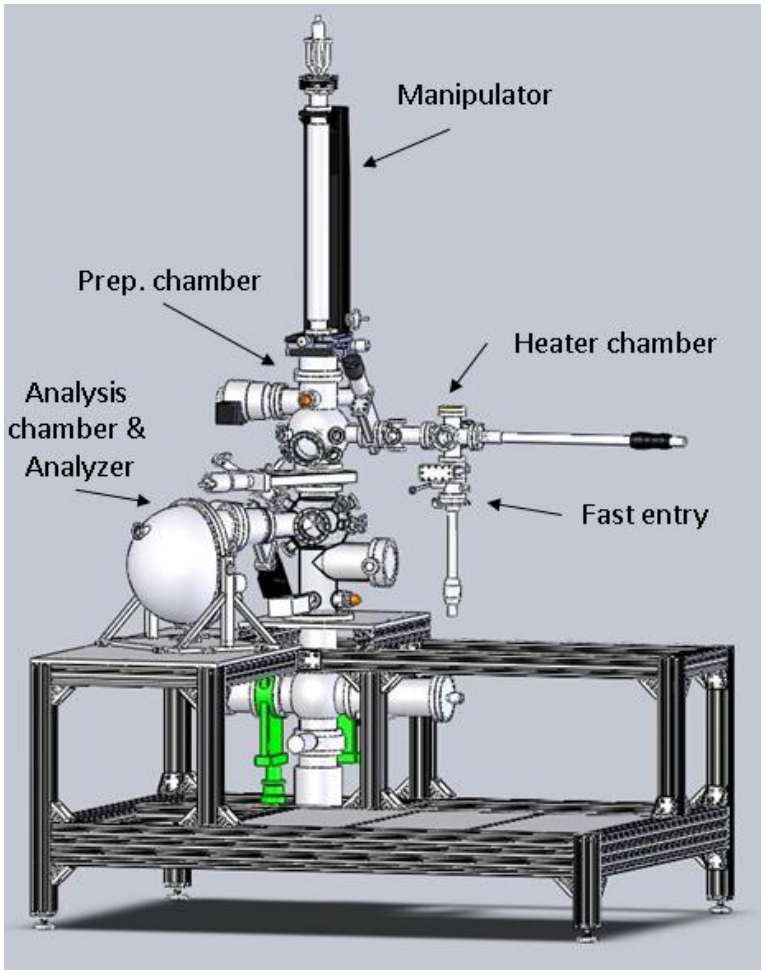

Figure 2.4: Schematicaly represented BaDElPh beamline end station at Elettra Sincrotrone (Trieste). Experimental set-up has vertical design with heater and preparation chamber mounted above measurement chamber for ARPES measurements while LEED optics is mounted on the bottom, inside the supporting structure. The whole system operates in UHV conditions and has transfer tools for *in-situ* sample preparation and studies [25].

3 Preparation of the films

The ability to grow thin metal films, supporting QWSs is a major challenge, since the interface between the film and substrate must be abrupt and the film must display an atomically uniform thickness over hundreds of micrometers. These conditions are necessary to confine the film valence electrons in a quantum resonator and study them by ARPES, which is a space-averaging technique. Interface chemical intermixing and ill-defined film thickness are detrimental to the observation of QWSs. The conditions for preparing films of Fe, Yb and Gd on W(110) and Mo(110) have been determined. QWSs have been observed in the cases of Fe on W(110) and Mo(110), and of Yb on Mo(110).

3.1 Preparation of clean W(110) and Mo(110) surfaces

The tungsten and molybdenum samples used are single crystals having at least 99.99% purity. The (110) surface of the samples was cut with an orientation accuracy < 0.1 deg and mechanically polished to achieve a roughness better than 0.01 μm.

The samples were mounted on a tantalum sample holder that can be inserted in the UHV system, cooled down to 100 K and heated via electron bombardment up to 2300 K.

The Mo(110) substrate was prepared annealing the sample in O_2 atmosphere ($9x10^{-7}$mbar) at approximately 1000 K for about 10 min. Subsequently, the inlet of oxygen was stopped, the base pressure was recovered ($1x10^{-10}$ mbar) and a rapid annealing of few seconds (flash) was done to approximately 2000 K. The procedure was repeated several times until good crystalline quality and a clean surface was obtained.

A similar procedure was used for the preparation of W(110): annealing at 1100 K of the sample in O_2 atmosphere ($5x10^{-7}$mbar) with a final flash at about 2300 K.

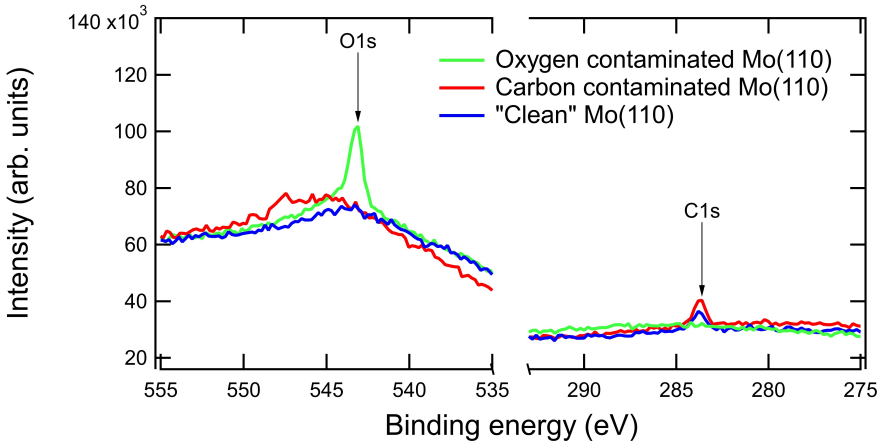

Figure 3.1: O and C 1*s* core level spectra measured on Mo(110) after flashing at T= 2000 K for removing O_2. In the case of T<2000 K the O_2 was not completely removed (green spectrum) while in the case of T>2000 K an increased amount of C contamination was detected (red spectrum). A good balance between oxygen desorption and carbon segregation was obtained after different cleaning cycles (blue spectra). The spectra were measured using 650 eV photon energy.

Carbon is a bulk contaminant of metals such as W and Mo. It tends to segregate to the surface when the temperature of the material is raised to crystallize the surface. The annealing in oxygen atmosphere is required for eliminating this C contamination. Oxygen reacts with carbon on the crystal surface forming CO. CO desorbs immediately since the crystal is at the temperature above that for CO desorption. Flashing Mo to 2000 K and W to 2300 K, after dosing oxygen, removes residual oxygen providing a clean surface. If the temperature is not sufficiently high, O residues are detected (Fig 3.1. green spectra) or, if it is too high, C starts to segregate from bulk to surface (Fig. 3.1. red spectra). To prepare a reasonably clean surface, the described procedure has to be repeated several times at optimal annealing conditions until a good balance between oxygen desorption and carbon segregation is obtained (Fig. 3.1. blue spectra).

LEED was used here together with XPS after each preparation step, to check whether the substrate surface was clean and well ordered. In the case of oxygen contamination we observed a 2x2 reconstruction of Mo(110) (see Fig. 3.2(a), small green spots in between 1x1 diffraction spots) while in the case of C contamination a complex LEED pattern was produced (Fig. 3.2(b)). Fig. 3.2(c) shows the LEED obtained for the clean Mo(110) where 1x1 diffraction spots are marked.

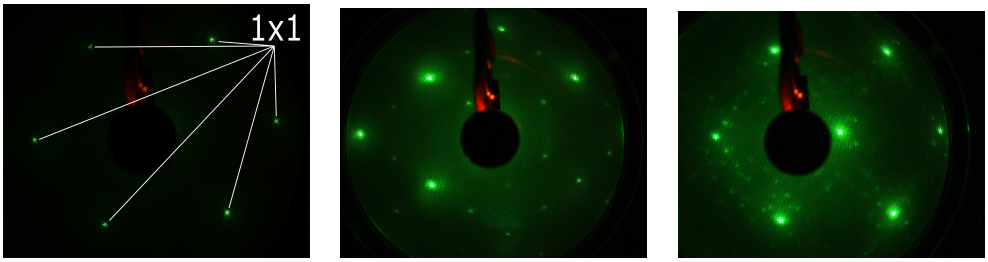

(a) (b) (c)

Figure 3.2: LEED patterns (Ep=70 eV) at the intermediate stages of Mo(110) sample preparation: (a) clean surface with 1x1 pattern, in the presence of (b) oxygen (pattern rotated for 90°) and (c) carbon contamination.

3.2 Growth of Fe films on Mo(110) and W(110) surfaces

Iron was evaporated on clean Mo(110) and W(110) surfaces using an electron beam evaporator (Omicron Triple) reported in Fig. 3.3. A rod of highly pure Fe (99.99%) was used and the evaporator was well outgassed to ensure deposition of clean Fe film in a pressure range of low 10^{-10}mbar. Before the preparation of the Fe films for the ARPES measurements (Paragraph 4.1), the stability and the optimal rate of evaporation were established by measuring the XPS core levels of Fe deposited on Mo(110) surface.

It is known from previous studies [26] that when Fe is evaporated on Mo(110) initially, independently of the rate of evaporation, the first monolayer is completed. For thickness larger than one atomic layer, at low deposition rates, the growth proceeds in a multi-layer fashion, while at high rates the layer-by-layer growth is partially preserved. In general, the growth mode of Fe on Mo (110) is the same as on W(110) at similar deposition rates [26]. Based on this knowledge, with the scope to find the condition for the preparation of epitaxial Fe film with uniform thickness, here below there is the description of how the optimal evaporation rate of Fe was found in order to obtain the layer growth regime.

Fig. 3.4 reports the XPS spectra measured for the clean Mo(110) surface and after three Fe evaporation using the same evaporator parameters. The high voltage applied to the rod was 1.25 kV and measured emission current was I_{em}=6.4 mA.

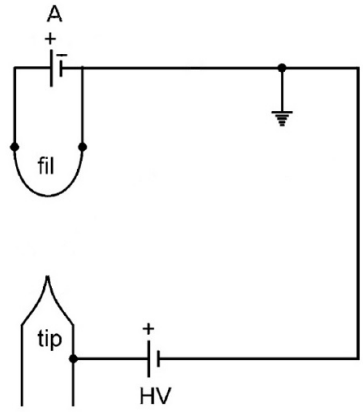

Figure 3.3: Schematic view of the Fe evaporator. A tungsten filament, placed in front of the tip of a high purity Fe rod, emits electrons which are attracted by the tip kept at high positive voltage. This electron current is the emission current, which, multiplied by the value of the high voltage, gives the power used for the Fe evaporation. Different values of power correspond to different evaporation rates.

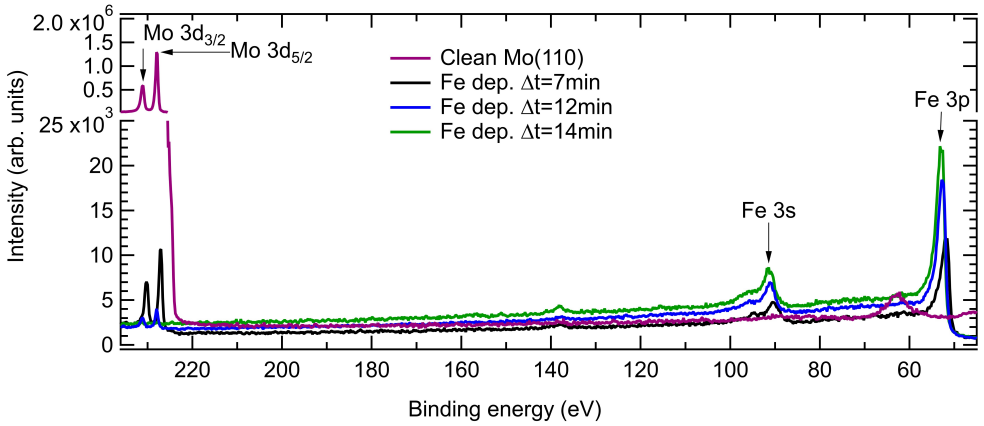

Figure 3.4: Core level spectra measured on clean Mo(110) surface and after three Fe evaporations of 7, 12 and 14 min. The depositions were done using the same evaporator parameters. The high voltage applied to the Fe rod was 1.25 kV and the measured emission current was I_{em}=6.4 mA. The spectra were measured using 650 eV photon energy.

Green spots in Fig. 3.5 represent the ratio of the integral area of Fe $3p$ and Mo $3d$ core level spectra shown in Fig. 3.4. The integral area is calculated after subtracting a linear background. The values of the integral area are normalized by the ionization cross section [27] that corresponds to the Fe $3p$ and Mo $3d$ core levels measured at photon energy of 650 eV.

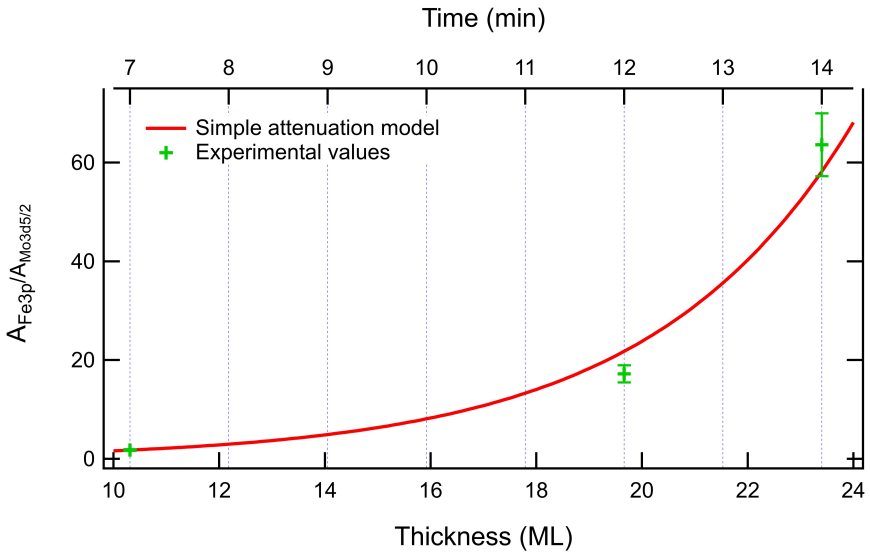

Figure 3.5: Ratio of the integral area of Fe $3p$ and Mo $3d$ core levels, normalized by the corresponding ionization cross section vs. deposition duration time (min) (green points). The red line is the expected ratio based on a simple attenuation model vs. thickness in ML (Formula 3.1).

The same graph also reports (red line) the expected ratio in the case of layer by layer growth, using a simple attenuation model (Eq. 3.1)[28].

$$\frac{A_{Fe}}{A_{Mo}} = \frac{\sigma_{Fe}}{\sigma_{Mo}} \frac{\sum_{i=0}^{n} \exp^{-i\frac{d_{Fe}}{\lambda_{Fe}}}}{\sum_{i=0}^{\infty} \exp^{-(i+n)\frac{d_{Mo}}{\lambda_{Mo}}}} \tag{3.1}$$

In this formula, A_{Fe} and A_{Mo} are the areas under Fe $3p$ and Mo $3d$ core level peaks, λ_{Fe} and λ_{Mo} are the inelastic mean free path of electrons (i.e. the distance an electron travels in a material, before it undergoes an inelastic scattering event) [29], d_{Fe} and d_{Mo} are the spacing between (110) atomic layers in Fe and Mo, σ_{Fe} and σ_{Mo} are photoelectron cross section at given energy [27] and "n" is the number of deposited atomic layers of Fe.

The three experimental values fit quite well with the ratio estimated for layer by layer growth mode (Fig. 3.5) and for this reason, for the growth of Fe films investigated by means of ARPES (Paragraph 4.1), the evaporator settings used are: U=1.25 kV and I_{em}=6.4 mA.

To improve the film quality with reduced roughness and higher crystalline order a post deposition annealing of the Fe films was performed. Our aim was to find an annealing procedure that produces better quality of the film without breaking the Fe film into islands. At RT we deposited approximately 24 ML thick Fe film on a clean substrate and measured the photoemission intensity map (Fig 3.6(a)). Fe valence states within 1 eV from E_F are visible but blurred. The measurement was repeated after each annealing step. The duration of the annealing was 10 min for all the investigated temperatures. Up to the annealing temperatures that correspond to resistive heating current of 20 A, the valence band features of the Fe film became sharper (Fig. 3.6(a)-(c)). This is an indirect indication of better crystalline quality of the film. For resistive heating current above 20 A the improvements on the photoemission maps are not so significant (Fig. 3.6(d)-(f)). Due to the absence of a thermocouple close to the sample, the value of the temperature during the annealing is not reported.

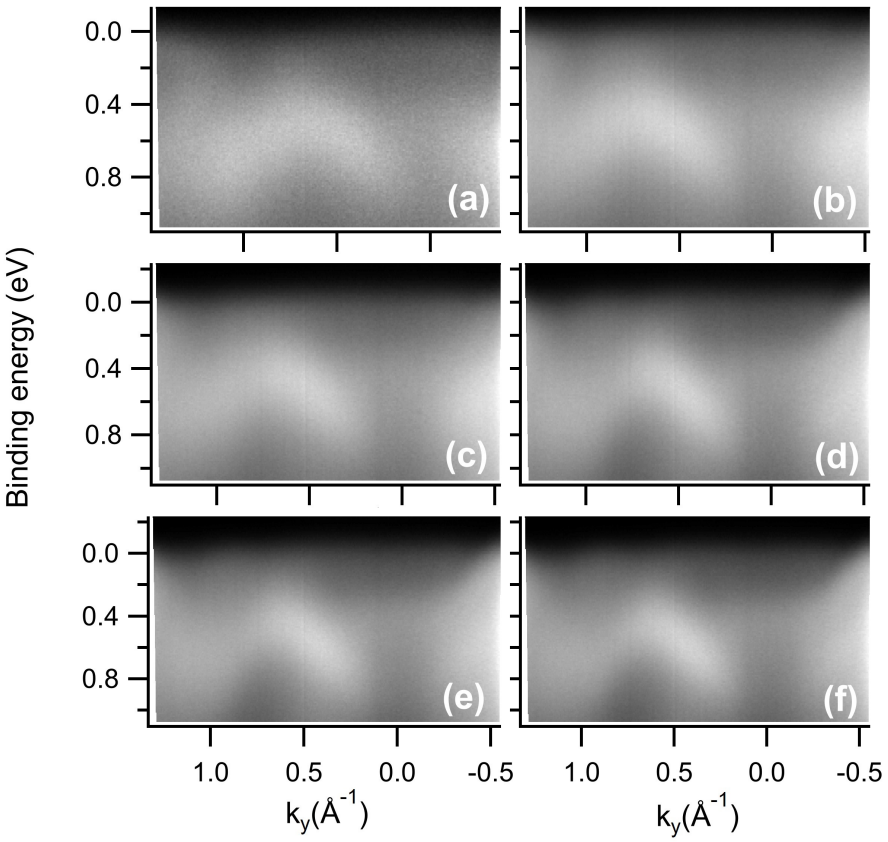

Figure 3.6: Photoemission intensity maps of a thick Fe film deposited at RT on Mo(110) and measured before (a) and after annealing using a resistive heating with current of (b) 15 A, (c) 20 A, (d) 25 A, (e) 27.5 A and (f) 30 A. The maps were measured using 55 eV photon energy.

To further study the stability of the Fe film upon annealing, the procedure described above was performed on an approximately 7ML thick Fe film. Fig. 3.7 reports the photoemission intensity maps measured after annealing with resistive heating currents of 20 A, 25 A and 27.5 A. All the maps initially present blurred bands that becomes sharper and sharper upon annealing. The quality of the photoemission maps improves up to 25 A (see Fig. 3.7(b)). Beyond that temperature, the appearance of a new feature, attributed to the Mo(110) substrate (Fig. 3.7 (c)), clearly indicates the breaking of the Fe film into islands. This test establishes that the annealing temperature must not exceed a temperature with resistive heating current through the sample of 20 A.

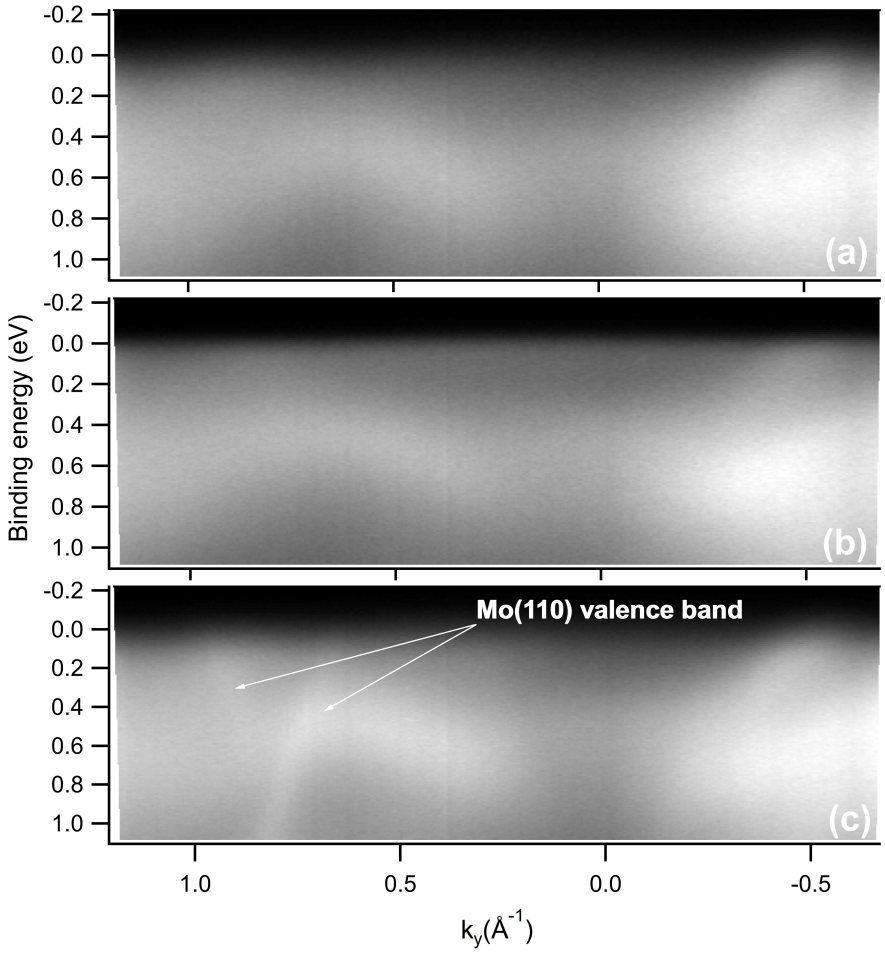

Figure 3.7: Photoemission intensity maps measured on a thin Fe film deposited at RT on Mo(110) (a) after annealing with resistive heating current of 20 A, (b) 25 A and (c) 27.5 A. The valence band states due to Mo(110) are indicated with arrows. The maps were measured using 55 eV photon energy.

3.3 Growth of Yb films on Mo(110) surface

The ytterbium deposition was done by using a home-made electron bombardment evaporator. Small pieces of pure Yb (99.99%) were placed into a tungsten crucible (see Fig. 3.8). Yb has a high vapour pressure and sublimate directly from the solid state. The material was degassed prior any deposition by keeping the crucible at an elevated temperature for several minutes until a base pressure better than $5x10^{-10}$mbar was obtained. The on-set and stability of the Yb sublimation was checked using a quartz microbalance and observing the increase of the base pressure. For the scope of the present work, an approximate calibration of the Yb coverage was done during the preparation of film as described below.

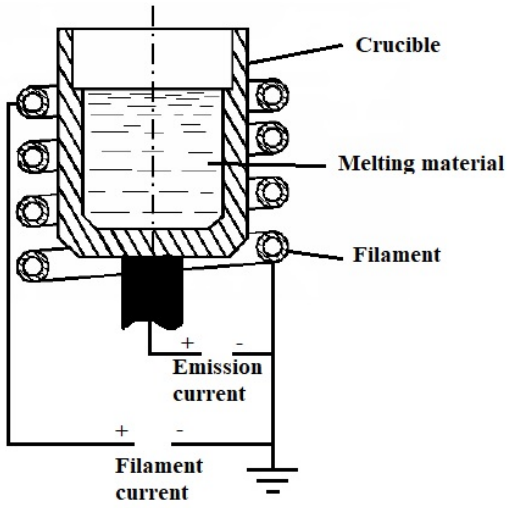

Figure 3.8: The in-house build Yb evaporator has tungsten round crucible in the middle with filament wire around. The crucible is heated by electron bombardment and the material inside is then sublimated on the sample.

Previous studies of Yb deposition on Mo(110) showed that multilayer Yb films are produced at RT [30, 31]. Initially, Yb forms complete layers on the W(110) and Mo(110) substrates. The layer-by-layer regime persists at least up to 4 ML. Fig. 3.9 reports the measured valence band spectra of three Yb films of different thicknesses A, B and C (RT deposition). The photoemission spectra for the thinnest film (A, green line in Fig. 3.9) shows three main features: one broad peak at 0.5 eV BE, one at 1.7 eV BE and one at 2.95 eV BE.

By increasing the Yb coverage to B, the broad peak at 0.5 eV disappears and new peaks appear at 0.1 eV BE, 1.3 eV BE, 1.75 eV BE, 2.55 eV BE, and 3.05 eV BE (red line in Fig. 3.9). For the highest coverage C the same peaks present at the coverage B are visible, but the peak at 0.5 eV BE becomes broader. The valence band structure of Yb film on Mo(110) surface was previously studied [31]. The broad peak at 0.5 eV BE (Interface) is attributed at the interface formed between Yb and Mo. The peaks at 1.7 eV BE and 3 eV BE (S) are associated to the $4f_{5/2,7/2}$ core level states emitting from the Yb atoms on the surface of the film (S) while the peaks

at 1.3 eV and 2.55 eV (B) are the $4f_{5/2,7/2}$ core level of Yb atoms emitting from the bulk of the film [31].

According to the literature [31], peak B appears only above a Yb coverage of 2 ML, otherwise the S and Interface peaks prevail. A more detailed study of the peak at 0.1 eV BE appearing for coverages B and C will be given in Chapter 4.2. Comparing the measured valence bands with that available in the literature [31], the estimated film thickness of sample A is of about 2 ML because of the absence of the peaks indicating bulk component (Yb $4f_{5/2}$(B) and Yb $4f_{7/2}$(B)). The coverages B and C correspond to thicknesses higher than 2 ML and we anticipate here that the feature at 0.1 eV BE has a fine structure that depends on the thickness and it will be described in the Paragraph 4.2.

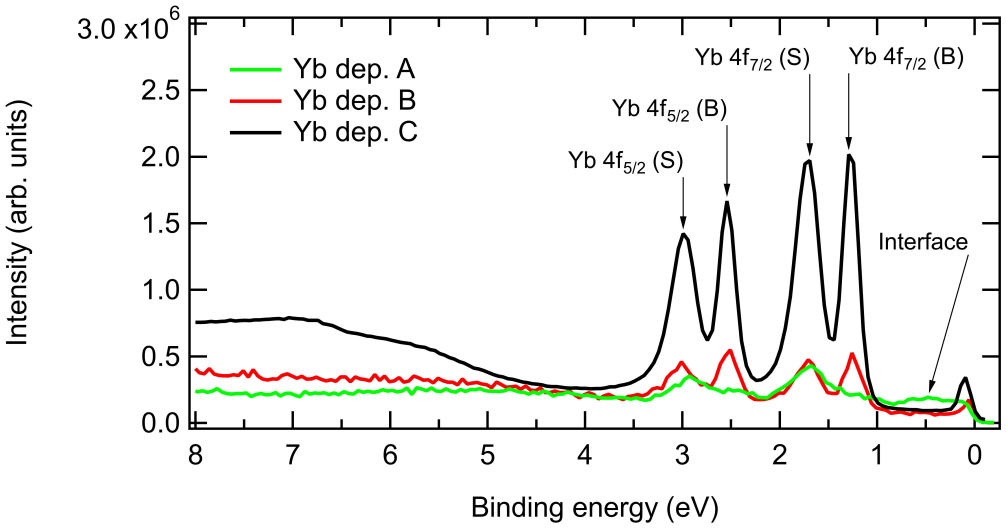

Figure 3.9: Valence band spectra after depositing, at RT, three different converges of A, B and C of Yb on Mo(110). Surface (S), interface (Interface) and bulk (B) peaks of Yb $4f$ core levels are indicated with labels [31]. The spectra were measured using 31 eV photon energy.

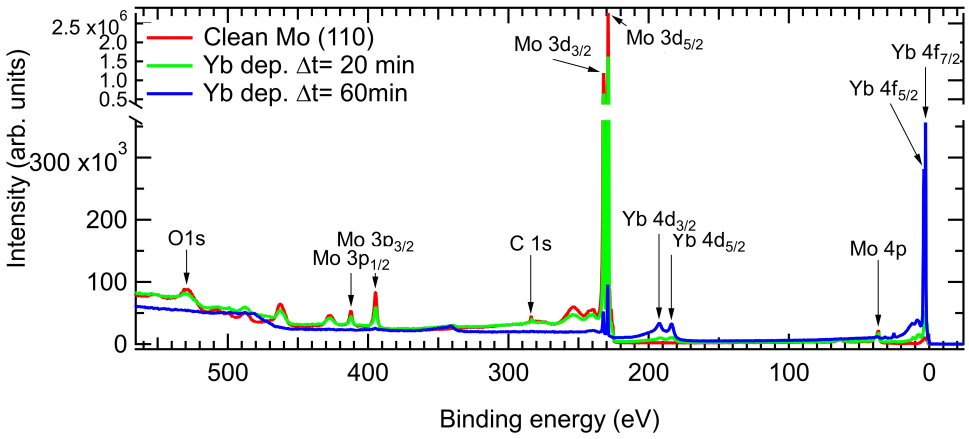

Figure 3.10: Photoemission spectra of clean Mo(110) substrate and after two subsequent evaporations of Yb. Low C and O contamination is observed. The spectra were measured using 650 eV photon energy.

In order to check the Yb film cleanliness and calibrate the Yb evaporation rate, Fig. 3.10 reports the photoemission spectra over a wide energy range. The deposition of Yb was performed with the Yb evaporator parameters at U=1.25 kV and I_{em}=1.4 mA. The duration of the two Yb evaporations were 20 min and 60 min respectively. After the first Yb deposition (Fig. 3.10, green line) there is a decrease of the Mo $3d$ core level signal while the Yb $4f$ peaks appears. After depositing 60 min of Yb there is a further decrease of Mo $3d$ peaks while Yb $4f$ becomes dominant in the spectra (Fig. 3.10, blue line). To fully suppress the substrate signal, the deposited film should be thicker than 3λ (3 times the inelastic mean free path or the distance an electron travels in a material before it undergoes an inelastic scattering event) which would be around 17 fully completed ML. Since the signal is still partially present the thickness of deposited Yb film is below this value.

For the study of the QWSs supported on thin Yb film, wedge shaped deposition was used for the preparation of film with different thicknesses. Wedged film can be constructed by varying the deposition time across the substrate surface with a use of a shield (Fig. 3.11).

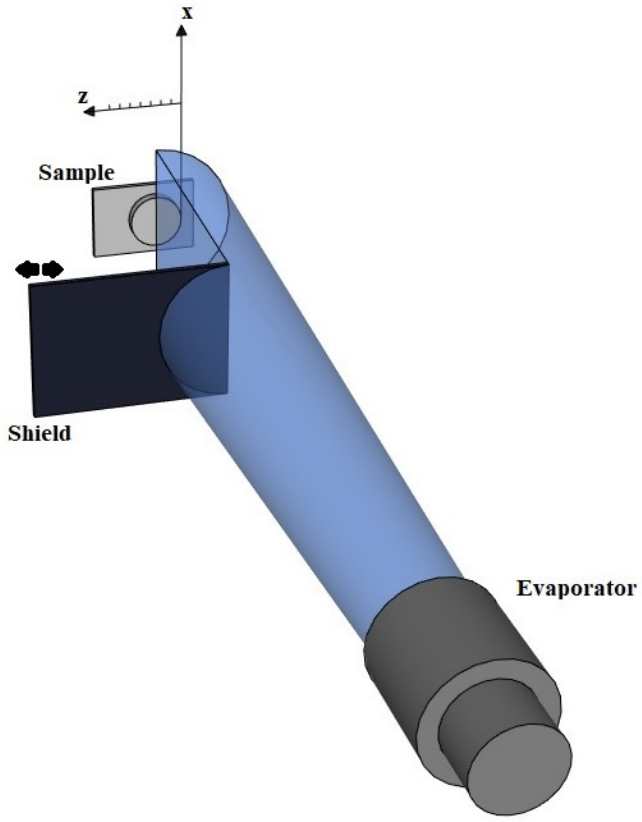

Figure 3.11: Schematic view of system used for wedged Yb film deposition on Mo(110).

The evaporation rate of the evaporator was monitored with a quartz microbalance before the deposition while the parameters used for this Yb wedge growth were U=1.25 kV and I_{em}=1.8 mA. During the Yb evaporator degassing and warming up, the Mo(110) substrate was fully covered by a shield. For the wedged Yb film growth, the shield was gradually removed in 6 equal steps (Fig. 3.11, positive z direction), each lasting for 7 min. With one side of the sample being longer exposed to the evaporator than the other, the film surface has a gradient and looks like a "wedge". In this way we are able to probe different film thicknesses with a single deposition sequence.

3.4 Preparation of Gd films on W(110) surface

The Gd evaporator was fabricated using the same design as for Yb. A tungsten crucible was filled with highly pure Gd (99.95%) pieces and heated with electron bombardment. The evaporator was thoroughly degassed before the Gd film growth at a base pressure of 1x10^{-9}mbar.

Gd deposited at RT on W(110) grows in a multilayer mode [32]. With scanning tunnelling microscopy (STM) it was observed that annealing at 530 K a Gd films, deposited at RT produces smooth films with terraces separated by monotomic steps [32]. Instead, Gd films annealed to 710 K, give rise to large 3D islands with quasihexagonal symmetry and relatively uniform size and a wetting monolayer (Stranski-Krastanov growth mode) [32]. By using Auger electron spectroscopy it was reported that Gd films deposited on the W(110) substrate held at a temperature between 723 - 773 K grow in the Stranski-Krastanov (SK) mode [33]. After the completion of few monoatomic layers, 3D islands start growing. The focus here was to find the experimental conditions for growing uniform and epitaxial thin films of Gd on W(110) substrate for a wide range of coverages. For this purpose we adopted the so called 'two-step growth', a method that was able to successfully produce smooth and uniform thick film of Ag on semiconductors. Thin films of Ag on Si(100) displaying QWSs, are obtained by deposition of Ag on the substrate at low temperature (130 K) and mild annealing up to 300-400 K [34]. Here we investigated with XPS, LEED and ARPES the possibility of obtaining an atomically uniform film of Gd displaying QWSs by depositing Gd on W(110) at 88 K and subsequently annealing it at different temperatures.

Two Gd films were prepared: A and B. All the ARPES, XPS and LEED measurements reported in this paragraph were done at T=88 K. Film A was prepared by evaporating Gd for 60 min on W(110) at T=88 K with evaporator settings U=1.25 kV and Iem=35 mA. The same film was subsequently annealed at 380 K, 645 K, 795 K. The core level spectra measured on the clean W(110) substrate, after the evaporation of Gd film at T=88 K, and after the different annealing temperatures are reported in Fig. 3.11. Upon Gd film deposition, the signal of the W $4p$, $4d$ and $4f$ core levels is completely quenched and does not appear after annealing up to 795 K. This result indicates that the Gd film covers the substrate and that the annealing, to this temperature, does not cause the breaking of the film into 3D islands. A very qualitative estimation of the Gd coverage can be obtained using the simple attenuation model (Formula 3.1). Based on this model, which assumes a layer by layer growth mode, the thickness of Gd necessary to fully suppress the W core level signals should be of about 15 ML.

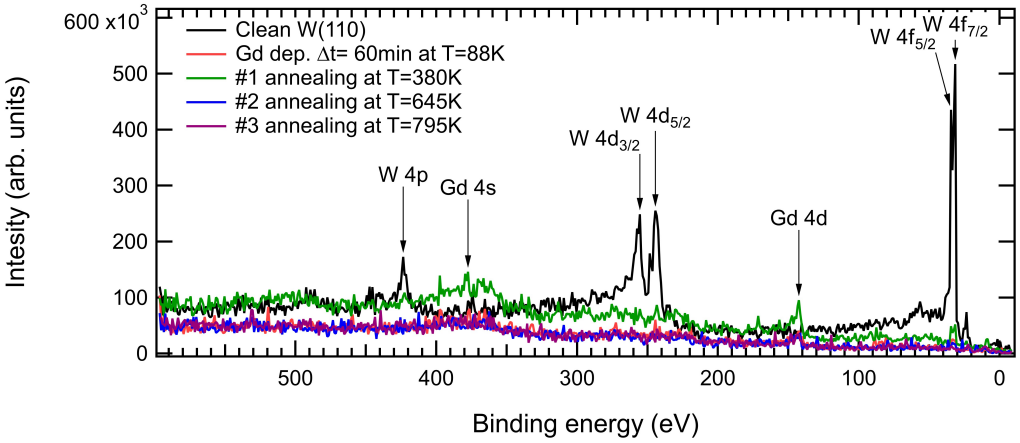

Figure 3.12: Core level spectra measured on clean W(110) surface and after 60 min Gd deposition (film A) and different subsequent annealings at 380 K, 645 K, 795 K. The spectra were measured using 1253.6 eV photon energy.

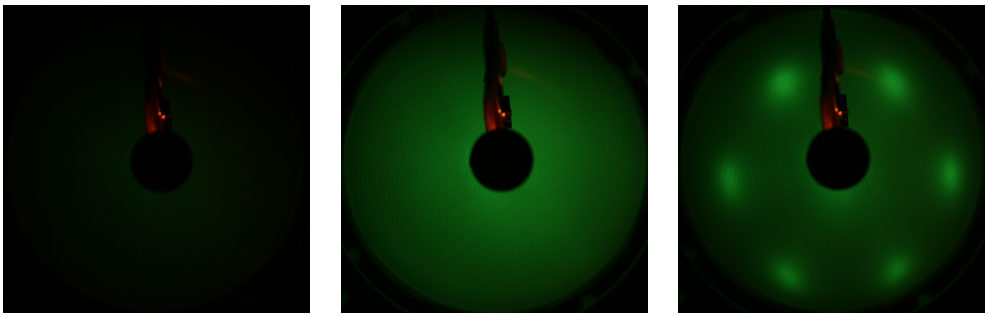

(a) (b) (c)

Figure 3.13: LEED patterns (Ep=70 eV) acquired after depositing 60 min of Gd on W(110) (film A) measured (a) as deposited and after subsequent annealing at temperature (b) T=645 K and (c) T=795 K.

After different annealing steps, the crystalline order of the film was monitored by LEED (see Fig. 3.13). A faint hexagonal pattern was detected after the annealing at 795 K. To check if the obtained Gd film was supporting QWSs photoemission intensity map reported in Fig. 3.14 were measured. No dispersing features were observed.

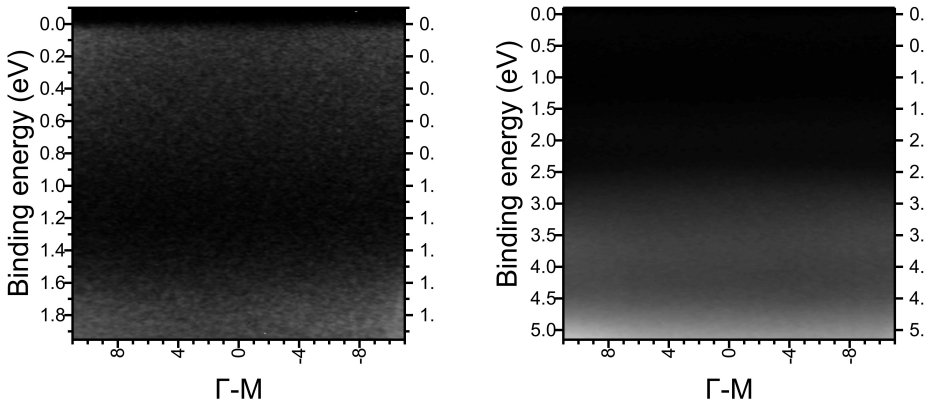

Figure 3.14: Photoemission intensity maps measured on a Gd film A, deposited at T=88 K on W(110) and subsequently annealed at T=795 K. Map (a) measured in the region of 2eV BE while map (b) in the wider region of 5eV BE. The maps were measured using 33 eV photon energy.

A second Gd film (film B) was prepared by evaporating Gd for 90 min (U=1.25 kV and I_{em}=37 mA) on W(110) at T=84 K with subsequent annealing at T=795 K. In Fig 3.15 are reported the XPS spectra at the different steps of the preparation of the film B. After the Gd deposition, the W core levels were suppressed, while after annealing to T=795 K the substrate signal reappears. This indicates the breaking of the film into 3D islands. Since the annealing temperature used in this case was the same as for film A, the film breaking can be due to the fact that the thickness of film B is lower than that of film A.

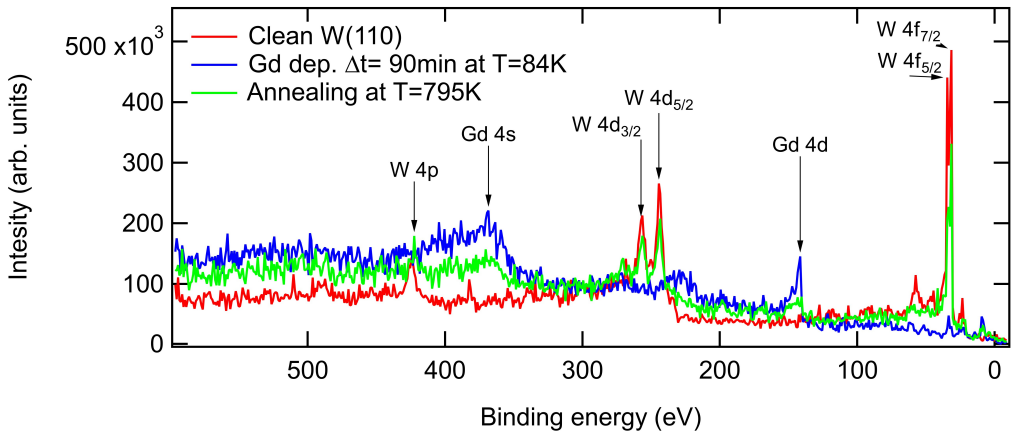

Figure 3.15: Core level spectra measured on clean W(110), after depositing for 90 min Gd (film B) at 88 K and after annealing up to 795 K for 10 min. The spectra were measured using 1253.6 eV photon energy.

Fig 3.16 reports the valence band spectra measured on clean W(110), after Gd deposition and after annealing to T=795 K. For the clean W(110) substrate the spectra shows strong W 5*d* peaks just below Fermi level. After the Gd deposition, the substrate peaks were suppressed. We can identify Gd 5*d* core level peaks at 8.5 eV BE. With annealing up to T=795 K a weak signal from the substrate appears just few meV below Fermi level together with a peak at 2 eV BE. The observation of these two peaks is another indication of the film breaking into 3D islands.

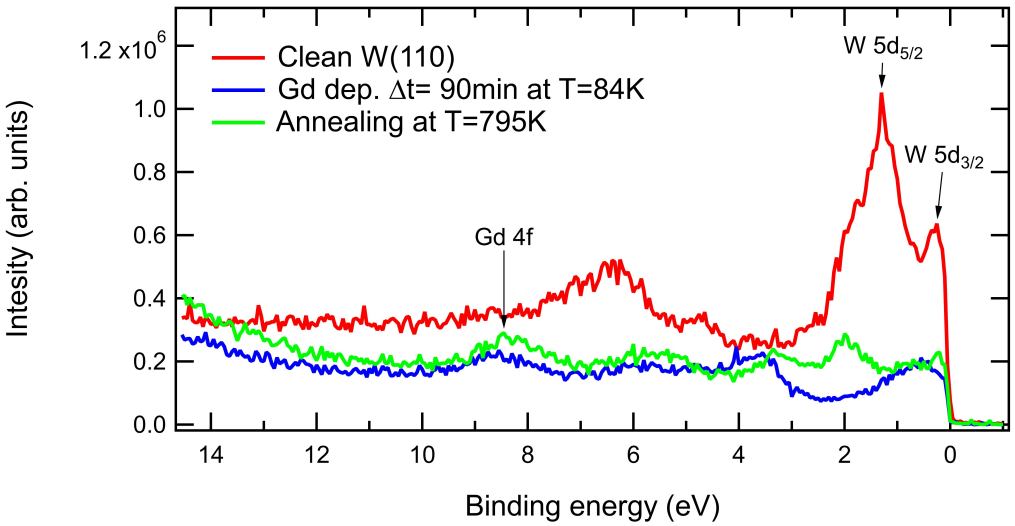

Figure 3.16: Valence band spectra measured on clean W(110) after depositing 90 min of Gd film at 88 K and after annealing the film up to 795K for 10 min. The spectra were measured using 33 eV photon energy.

After the annealing of film B at T=795 K the crystalline structure of the film was checked (see Fig. 3.17). The observed LEED pattern resembles that obtained overlapping faint hexagonal, coming from the substrate, and a 5x2 pattern, associated to the deposited Gd film, which are incommensurate. In literature it was previously reported that for films of 0.6 ML coverage of Gd on W(110), the LEED pattern is 5x2 [35]. For higher coverages (above 0.6 ML) the pattern is hexagonal. This is yet another indication that the annealing causes a film breaking and that there could be a submonolayer coverage of Gd, contributing with the (5x2) pattern, on top of which there are 3D islands (hexagonal pattern).

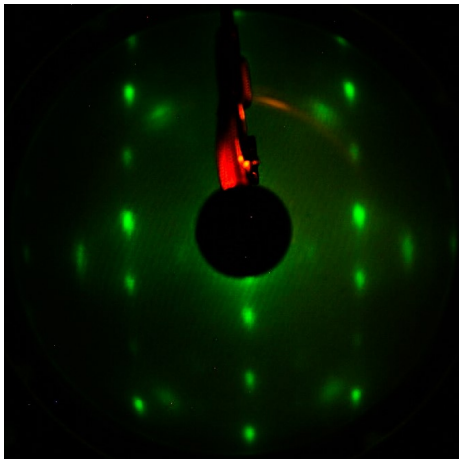

Figure 3.17: LEED pattern (Ep=70 eV) acquired after annealing the film B of Gd up to T=795 K. Incommensurate hexagonal and a 5x2 pattern are observed simultaneously.

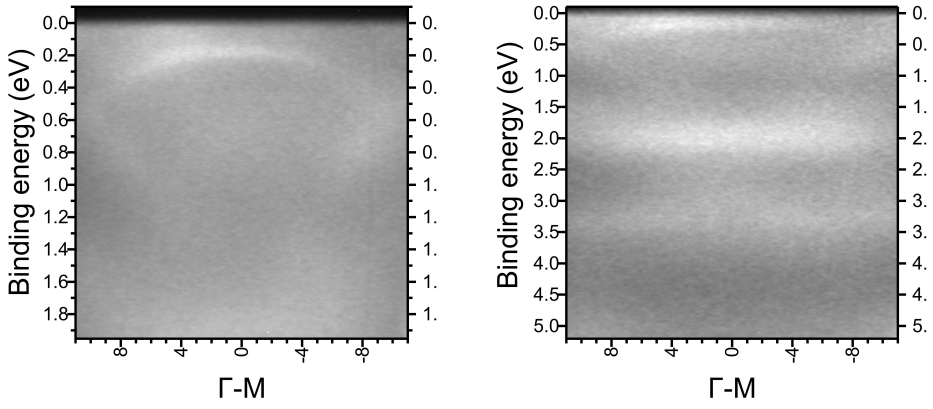

(a) (b)

Figure 3.18: Photoemission intensity map measured on film B after the annealing up to T=795 K. Map (a) measured in the region of 2eV BE while map (b) in the wider region of 5 eV BE. The maps were measured using 33 eV photon energy.

Fig. 3.18 reports the photoemission intensity maps measured on the film B after the annealing. The features present in the maps originate from the substrate as already observed in the valence bands reported in Fig. 3.16. In conclusion, none of the investigated procedure for the growth of Gd film on Mo(110) resulted in the formation of a uniform film supporting QWSs.

4 Electronic structure characterization of the metal films

This Chapter presents the characterization of the electronic structure of Yb films on Mo(110) and of Fe films on W(110) and Mo(110). For these heterostructures, as described in Chapter 3, it was possible to find a procedure for obtaining films possessing atomically homogeneous thickness in the order of few nm. The characterization has been done by means of ARPES and the observation of QWSs is discussed.

4.1 Yb on Mo(110)

Electron confinement effects in Yb films on W(110) were discovered by means of low temperature scanning tunnelling spectroscopy (STS) [37]. In Chapter 3 we optimized the growth of atomically homogeneous Yb films on Mo(110) over macroscopic areas. This allows us to use a non-local spectroscopy technique such as ARPES in order to characterize the electron confinement effects onto the electronic structure.

By utilizing the wedge deposition technique, described in Paragraph 3.3, homogeneous Yb films, with different thicknesses, were prepared on the Mo(110) substrate. The preparation of the films in the form of a wedge ensures the same growth conditions for films of different thicknesses with a single preparation step.

Fig 4.1 (a) reports the 2D intensity map measured on an Yb film on Mo(110). The map is measured along the high symmetry direction $\overline{\Gamma M}$. The surface Brillouin zones and high-symmetry directions of Yb(111) (black line) and Mo(110) (green line) are reported in Fig. 4.1 (d). In the 2D intensity map of Fig. 4.1 (b), three parabolic (nearly-free electron) like electronic bands are visible near $\overline{\Gamma}$, $\overline{M}$ and in the range of k_y between 0.3 and 0.8 Å^{-1}. The features are indicated with coloured dots in the map and correspond to QWSs of the Yb film. These electronic states can be seen also in the EDC extracted from the 2D intensity maps at $\overline{\Gamma}$ (c) and k_y=0.6 Å^{-1} (b), where they appear as peaks (coloured dots).

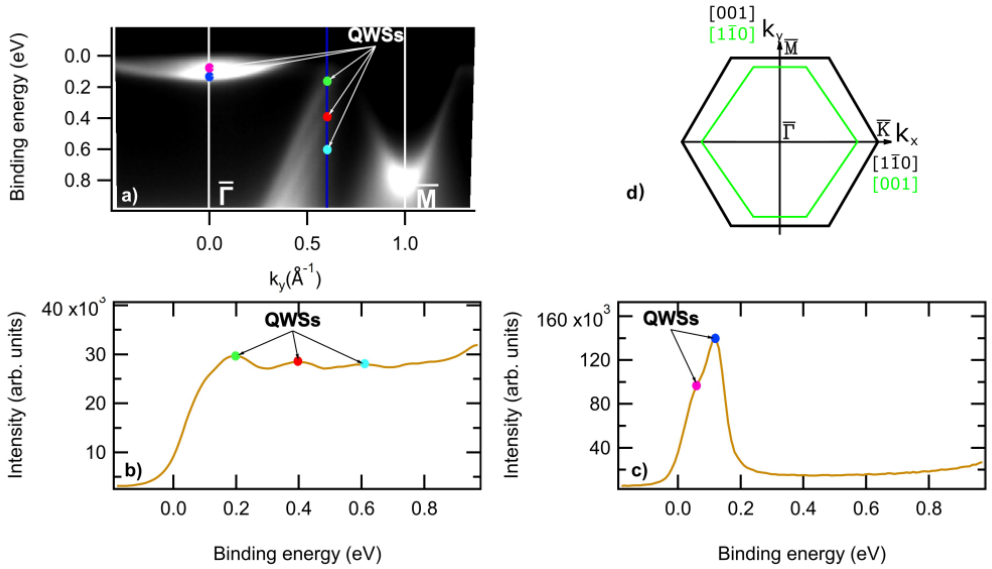

Figure 4.1: (a) 2D photoemission intensity map measured on a Yb film, grown on Mo(110), along the $\overline{\Gamma M}$ direction. (b) and (c) are EDCs extracted from the the 2D map of Fig. 4.9 (a) at k_y=0.6 Å^{-1} and k_y=0 Å^{-1} respectively. (d) Surface Brillouin zones and high-symmetry directions of Yb(111) (black line) and Mo(110) (green line).

As mentioned in Chapter 1, a more rigorous characterization of QWSs requires their study as a function of film coverage. Fig. 4.2 reports the second derivative (along the energy axis) of the 2D photoemission intensity maps measured at different positions of the Yb wedge grown on Mo(110) (see Fig. 4.2 ((a) - (j)). The map (a) corresponds to the thinnest side of the wedge while the map (j) corresponds to the thickest one. In all maps three main groups of nearly-free electron-like dispersive states are observed. In the k_y range between 0.3 and 0.8 Å^{-1} the number of states increases as a function of the film thickness and their energy separation decreases. The number of the states centred at $\overline{\Gamma}$ increases with the film thickness while their minimum moves towards higher BE. The parabolic band centred at $\overline{M}$ shows no clear change with the film thickness.

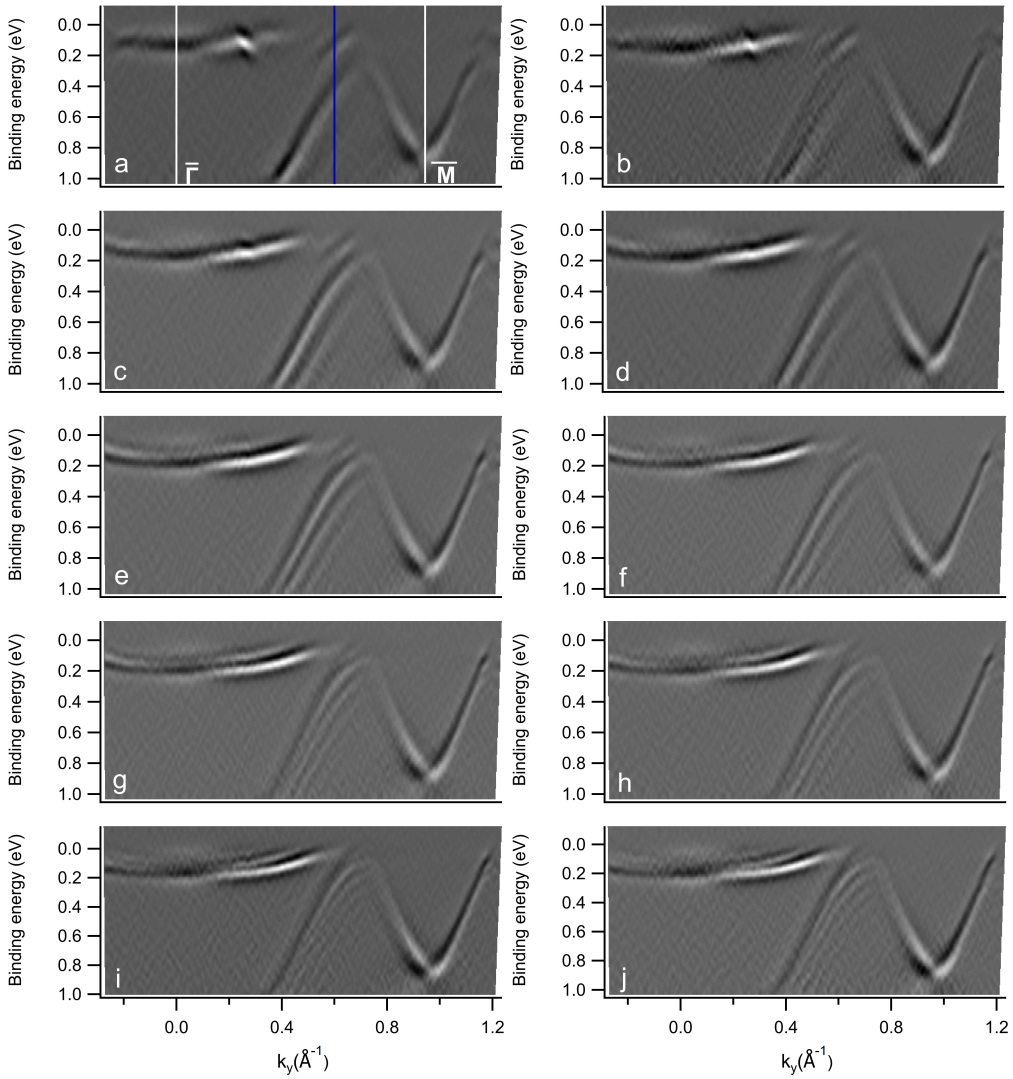

Figure 4.2: Second derivative of 2D photoemission intensity maps measured on Yb/Mo(110) along $\overline{\Gamma M}$ direction. (a)-(j) indicate different measurement position on the film wedge of Yb. The different positions correspond to different film thickness and going from (a) to (j) the thickness increases. All maps were measured using 35 eV photon energy.

To better understand the features in the k_y region between 0.3 and 0.8 Å^{-1}, Fig 4.3 reports the EDC extracted from the 2D intensity maps of Fig. 4.2, at k_y=0.6 Å^{-1} (Fig. 4.2 (a), blue line). Going from the coverage (a) to (j), the energy separation between the peaks decreases by increasing the thickness of the Yb film (dots in Fig. 4.3).

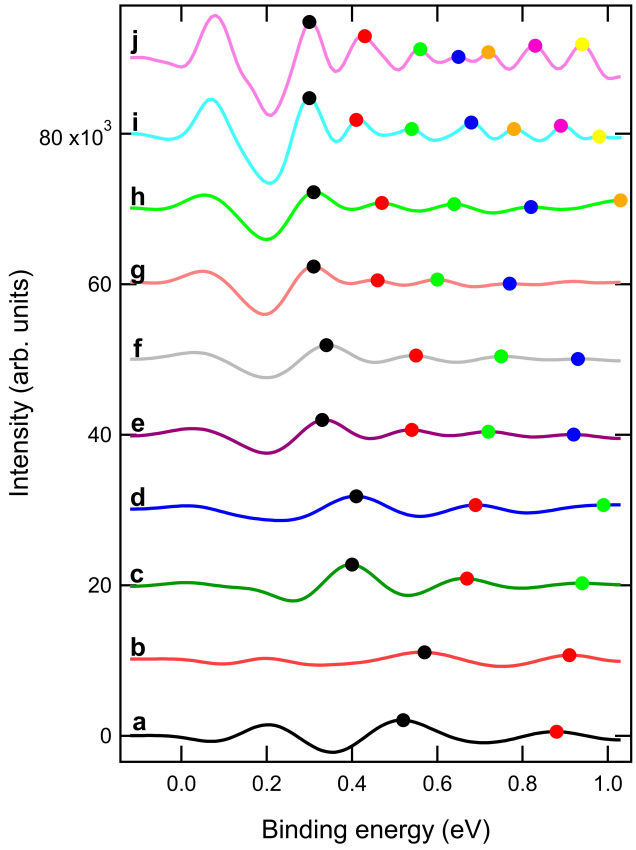

Figure 4.3: EDCs extracted at $k_y = 0.6$ Å^{-1} from 2D photoemission intensity maps reported in Fig. 4.2. Going from (a) to (j) the Yb film thickness increases.

A similar trend is also shown by the electronic features that are close to the E_F and disperse around $\overline{\Gamma}$. Fig 4.4 reports the EDCs extracted from the 2D intensity maps of Fig. 4.2 at $\overline{\Gamma}$ (k_y=0). On the thinner part of the wedge ((a) – (c)) one state is present (Fig. 4.3 black dot). For film thicknesses between (d) and (f) there is a second state (Fig. 4.3 red dot), at lower BE than the first state observed in (a) - (c). For thicknesses above (f) a third state (Fig. 4.3 blue dots) appears at lower BE with respect to the previous two states. By increasing the coverage, all the three states move to higher BE and their energy separation decreases.

This behaviour demonstrates that the observed features correspond to QWSs of a thin metallic film (Chapter 1). As mentioned above, electron confinement effects of Yb thin film were observed previously for Yb(111) films deposited on W(110) [37]. STS spectra presented sharp peaks due to the formation of QWSs [37]. Although there is no band gap in Mo(110) (or W(110)) at below (above) E_F, the hybridization of states at $\overline{\Gamma}$ is small due to different symmetries of the electronic states ($\overline{\Gamma L}$) and therefore electron confinement effects can take place. The fact that the measured band structure of Yb films on Mo(110) possesses QWSs, over a wide range of thicknesses, establishes that the film of Yb on Mo(110) is uniform and QWSs provide a way to establish the absolute thickness of the film.

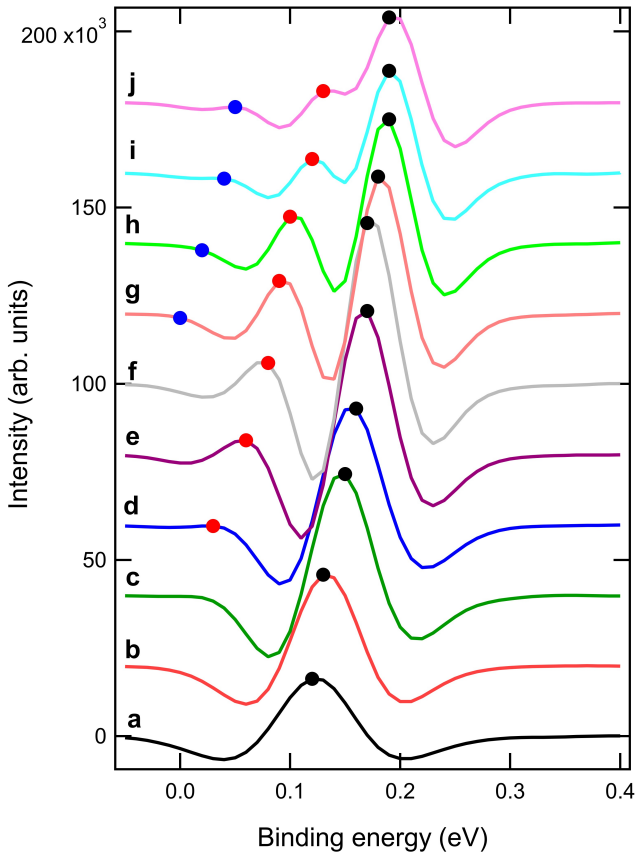

Figure 4.4: EDCs extracted from 2D photoemission intensity maps reported in Fig. 4.2 at $\overline{\Gamma}$ (k_y=0). Going from (a) to (j) the Yb film thickness increases.

As the quantum well peak positions had been determined for a number of different film thicknesses, one could obtain the bulk band structure $E(k)$ [15] or the film thicknesses can be obtained by comparing the peak positions (or their energy differences) with modelled band structure [15].

Based on this, the Yb film thickness corresponding to the measured films (a) - (j) is evaluated as follows. Firstly, the energy separation between the different states dispersing in the k_y region between 0.3 and 0.8 Å^{-1} is calculated. For this purpose, for each coverage, we extracted from the 2D intensity maps of Fig. 4.2 three EDCs at k_y=0.65 Å^{-1}, k_y=0.6 Å^{-1} and k_y=0.7 Å^{-1}. The energy separation between the peaks (ΔE_{exp}) is obtained, for each coverage, by averaging the energy separation obtained from the EDC at k_y=0.65 Å^{-1}, k_y=0.6 Å^{-1} and k_y=0.7 Å^{-1}. The resulting values of ΔE_{exp} for each coverage are reported in Tab. 4.1.

Recent Density Functional Theory (DFT) calculations were performed with the plane wave pseudopotential code Quantum-ESPRESSO employing the Perdew-Burke-Ernzerhof (PBE) functional for the exchange and correlation energy and ultrasoft pseudopotentials [38]. The calculations considered Yb slabs of 7 ML, 14 ML and 21 ML. Here this modelled band structure [38] is used with the scope of calibrating the Yb film thickness. From the calculated electronic band structure [38], we obtained the theoretical energy separation (ΔE_{th}) at k_y=0.65 Å^{-1} between states of three different thicknesses. In Fig. 4.5 the ΔE_{th} values vs thickness are presented with circular

markers. The red line in Fig. 4.5 is the result of the fit of ΔE_{th} values with a quadratic function. The theoretical energy differences (ΔE, red line) between QWSs as a function of coverage is reported in the graph of Fig. 4.5 for coverage in the range between 5 ML and 40 ML. By comparing the ΔE_{exp} values with the ΔE curve, we obtained the thicknesses corresponding to (a) - (j) measurement positions on the Yb film wedge. The values (Thickness) are reported in Tab. 4.1.

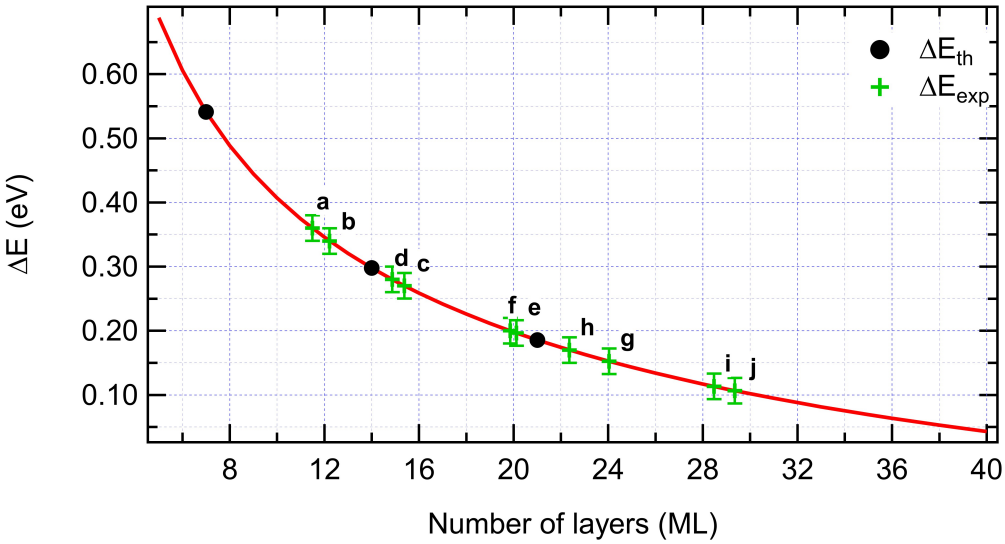

Figure 4.5: Circular markers are the energy separation (ΔE_{th}) between QWSs extracted from calculation of valence band structure done for 7, 14 and 21 ML of Yb on Mo(110) [38]. The red line is the fitting curve of ΔE_{th} values and represent the theoretical energy (ΔE) separation of QWS of Yb films on Mo(110). Cross markers are the ΔE_{exp} calculated from the experimental EDC reported in Fig. 4.3. (a)-(j) indicate the different film thicknesses as described in the text.

In Tab. 4.1, we observe that the couple of positions (a)-(b), (c)-(d), (e)-(f), (g)-(h) and (i)-(j) have the same ΔE_{exp}, within the experimental error. This is consistent with the fact that the measurements for those coupled positions were deliberately acquired on parts of the film wedge having the same thickness.

Table 4.1: Calculated ΔE_{exp} as a function of different measurement position ((a)-(j)) on the Yb film wedge. The Thickness in ML has been calculated by comparing the ΔE_{exp} with the expected ΔE (red line in Fig. 4.12) following the procedure described in the text.

	ΔE_{exp} (eV)	Thickness (ML)
a	0.36 ±0.02	11.5
b	0.34 ±0.02	12.2
c	0.27 ±0.02	15.4
d	0.28 ±0.02	14.9
e	0.20 ±0.02	20.1
f	0.20 ±0.02	19.9
g	0.15 ±0.02	24.0
h	0.17 ±0.02	22.4
i	0.11 ±0.02	28.5
j	0.11 ±0.02	29.3

The nature of the observed electronic states of Yb film on Mo(110) is now discussed comparing the experimental data (see Fig. 4.2) with published calculations [39].

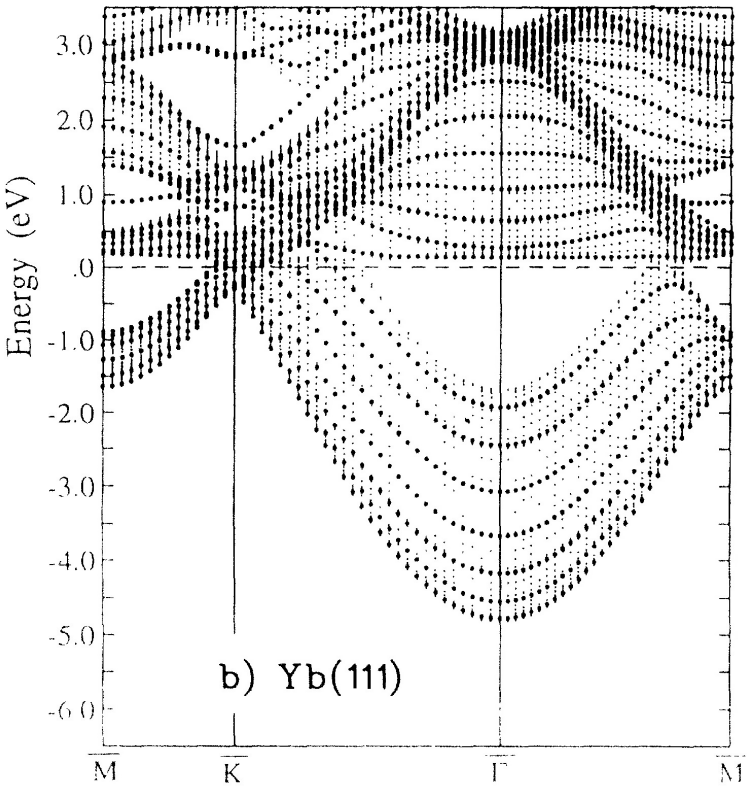

Figure 4.6: Calculated band structure in the surface Brillouin zone of a 7 ML slab (large dots) superimposed on the projected bulk bands (dashed) for Yb(111) surface [39].

LDA scalar relativistic band structure calculations [39] are reported in Fig. 4.6. The calculated band structure shows the presence of two nearly free-electron like bulk bands that are s-derived. One band disperses between the $\overline{\Gamma}$ and $\overline{K}$ points with a total width of about 3 eV, while another band is between $\overline{K}$ and $\overline{M}$ with a total width of about 1 eV. These two occupied s-like bands are composed by seven subbands. The energy difference between the subbands is of few hundred of meV from $\overline{\Gamma}$ to $\overline{K}$, while it is of few tens of meV from $\overline{K}$ to $\overline{M}$. By comparing our experimental findings (Fig. 4.2) with the calculated electronic structure, we conclude that the measured states in the k_y range between 0.3 and 0.8 Å^{-1} correspond to the calculated electronic band from $\overline{\Gamma}$ to $\overline{K}$, while the measured parabolic state centred at k_y=0.95 Å^{-1} correspond to the calculated band form $\overline{K}$ to $\overline{M}$. As discussed above, the states measured in the k_y range between 0.3 and 0.8 Å^{-1} are QWSs. The measured QWSs correspond to the calculated subbands. Given the fact that our energy resolution of our ARPES measurements is of the order of few tens of meV we are able to measure the energy splitting of the subbands calculated from $\overline{\Gamma}$ to $\overline{K}$, but not that from $\overline{K}$ to $\overline{M}$. In fact, in the measured 2D photoemission intensity maps reported in Fig. 4.2, the parabola centred at k_y=0.95 Å^{-1} no variations are observed with film thickness.

Interestingly, the calculations [39] predict the presence of surface and QW states above E_F around $\overline{\Gamma}$ point (see Fig. 4.6). We observed occupied states below E_F in that region. The discrepancy can originate from the relative position of the Fermi level with respect to the highest occupied and empty subbands. We can not exclude that the observed states at $\overline{\Gamma}$ close to the Fermi level correspond to empty states that become occupied because of the energy shift of the E_F with the increase of the film thickness due to a small strain effects onto the Yb film. A different surface-charge distribution because of a slightly different unit cell dimension can result in different electronic band structure [40].

As mentioned in Chapter 1 the electronic structure of Yb films is not trivial. In fact, it has been shown that Yb films, grown at low temperature on W(110), possess an fcc crystal structure such as β Yb metal but with the d_{111} layer spacing reduced by 0.6% [30]. Such small structural variation can imply a variation of the electron occupancy of $4f$ orbitals and in turn the magnetic properties of the film [30]. The experimental electronic structure of Yb films here presented, and in particular the evolution of the QWSs, will be used in combination with LDA calculation to better explain the above mentioned open questions.

4.2 Fe on W(110) and Mo(110)

Homogeneous films of Fe on W(110) and Mo(110) substrates have been prepared and studied by means of ARPES in order to detect the presence of QWSs and characterize their behaviour as a function of energy, momentum and magnetization of the film. The results here obtained for Fe films on Mo(110) and W(110) extend the knowledge already acquired for Co films on Mo(110) and W(110) surfaces [17, 20]. We found that Co films on W(110) present magnetic QWSs states showing up an asymmetric band dispersion along equivalent crystallographic directions in contrast with the expectation for centro-symmetric systems [17]. Moreover, we demonstrated that the asymmetries can be reversed with respect to the centre of the Surface Brillouin zone by switching the in-plane magnetization of the Co films. These effects originate from the coupling of the exchange interaction of the magnetic films and the high spin-orbit coupling of the substrate [17]. For the case of Fe films discussed here we find again magnetic QWSs, but the band asymmetries are less clear.

The Fe films has been grown on W(110) and Mo (110) surfaces using the deposition technique described in the Paragraph 3.2. The electronic structure characterization was performed after the as-grown films were uniformly magnetized by a magnetic pulse generated by a coil near the sample surface.

To determine the orientation of the Fe film magnetization we measured the magnetic linear dichroism (MLD) of Fe $3p$ core levels [36]. In the present case, the MLD measurements were performed in the geometry displayed in Fig. 4.7. The yellow circle represents the sample where k_y is parallel to the Fe[1-10] axis and k_x is aligned with Fe[001] axis. The light scattering plane (grey semicircle) is either parallel or perpendicular to Fe[001] direction (Fig 3.19(a) and (b) respectively). The polarization of the photon beam is horizontal.

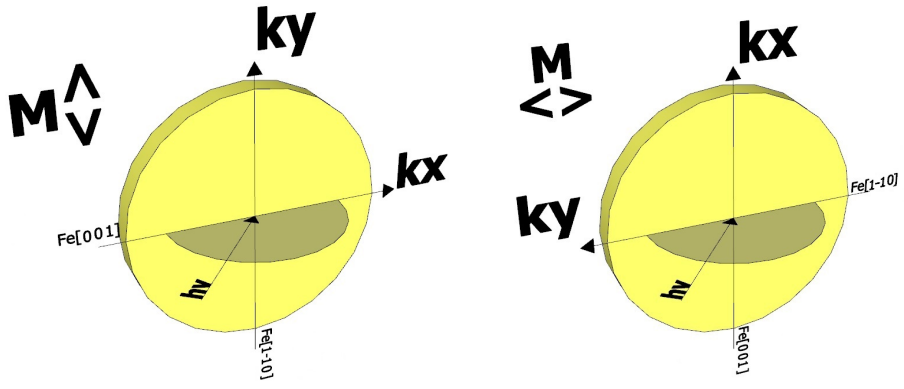

(a) (b)

Figure 4.7: (a) MLD measuring geometry for sample magnetization along k_y axis that represents Fe[1-10] direction while light scattering plane is in k_x or Fe[001] axis. (b) The light scattering plane is now aligned with the magnetization direction in k_y or Fe[1-10] axis. Photon beam polarization is horizontal, parallel to light scattering plane.

The Fe $3p$ core level spectra in Fig. 4.8((a), (b)) are collected in two different measurement geometries. The spectra in Fig. 4.8 (a) have been acquired with sample magnetization orientation pointing towards positive and negative k_y values (M$\triangle$ and M$\triangledown$ respectively) with light scattering plane perpendicular to the sample surface. The spectra measured are different and there is MLD. In the second case (Fig. 4.8 (b)) the light scattering plane is aligned with the magnetization direction, the spectra are the same and the MLD is zero. These measurements confirm that the Fe films are magnetized in plane along the Fe[1-10] axis, as expected from [41].

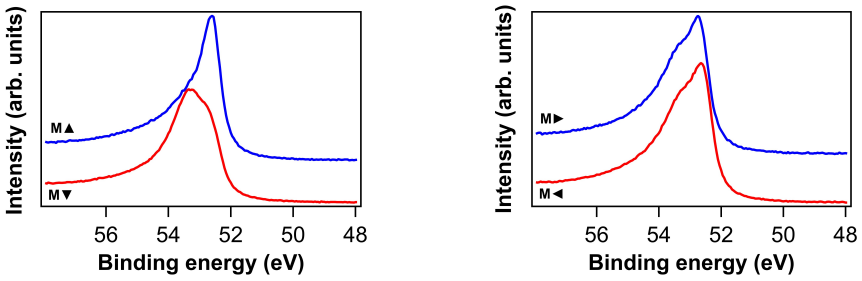

(a) (b)

Figure 4.8: Fe $3p$ core level photoemission spectra measured with the scattering plane perpendicular (a) and parallel (b) to the magnetization direction. Magnetic dichroism is visible only in the first case. The spectra are measured using 130eV photon energy.

In Fig 4.9 the surface Brillouin zones (BZ) of Fe(110), W(110) and Mo(110) are reported together with high symmetry axes. The surface BZ of the substrates (red line for W(110) and green line for Mo(110)) and of Fe(110) film (black line) present the same shape and differ in size.

The electronic properties of Fe film on W(110) were studied on a uniform and homogeneous film having a thickness of 10 ML. Fig. 4.10(a) reports the 2D photoemission intensity map acquired along the high symmetry direction $\overline{\Gamma H}$ (k_x axis in Fig. 4.9). The measurements with negative values of k_x correspond to the magnetization "UP" while those with positive k_x correspond to the magnetization "DOWN". The sample was then rotated by 90° and the measurements were done along the $\overline{\Gamma N}$ direction (k_y axis in Fig. 4.9). In both maps the QWSs appear as dispersing electronic features having energy separation of few tens of meV. The QWSs are better resolved in the case of Fig. 4.10 (b) where their energy-momentum dispersion is also highlighted with colours.

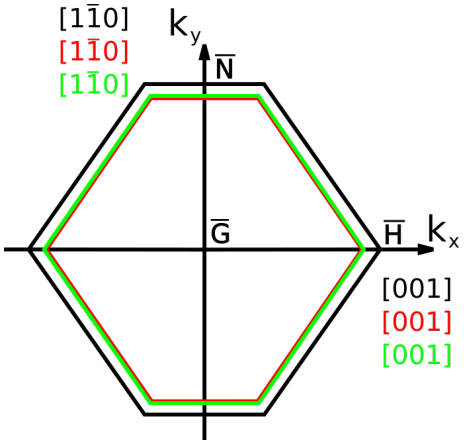

Figure 4.9: Surface Brillouin zones and high-symmetry direction of Fe(110) (black line), W(110) (red line) and Mo(110) (green line).

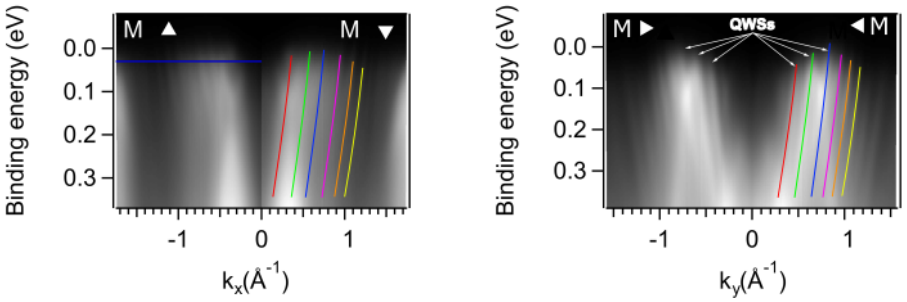

(a) (b)

Figure 4.10: 2D photoemission intensity maps measured on Fe film 10 ML thick deposited on W(110). The measurements were done (a) along the $\overline{\Gamma H}$ direction (k_x axis) and with the magnetization perpendicular to the scattering plane and (b) along the $\overline{\Gamma N}$ direction (k_y axis) with the magnetization in the scattering plane of the experiment. QWSs are highlighted by coloured lines. The photoemission maps were measured using 55 eV photon energy.

In order to understand the dispersion of the QWSs as a function of the $k_{x,y}$ momentum and of the magnetization of the film, Fig. 4.11 reports the MDC curves (Paragraph 4.1) extracted from the 2D photoemission intensity map of Fig. 4.10 (a) and (b) at BE= 30 meV (blue line in Fig. 4.10 (a)). In Fig. 4.11 (a) there is the MDC spectrum along the $\overline{\Gamma H}$ direction (k_x axis), while in Fig. 4.11 (b) it is along the $\overline{\Gamma N}$ direction (k_y axis). We observe a left-to-right asymmetry in Fig. 4.11(a), which is absent in Fig. 4.11(b). This can be ascribed to the coupling of exchange and Rashba interactions, as in the case of Co/W [17].

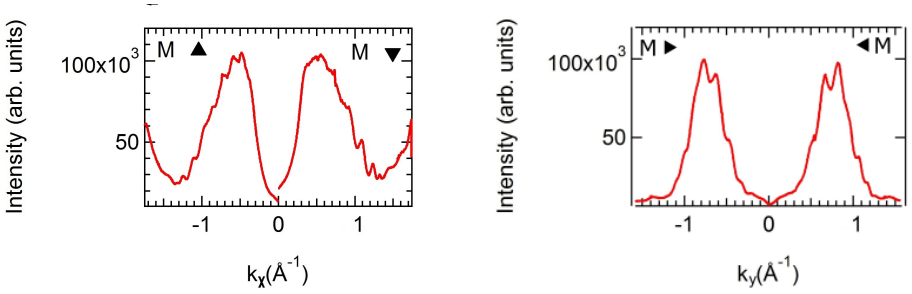

Figure 4.11: MCDs extracted, at 30 meV, from the 2D intensity maps of Fig. 4.10. The MCD cuts are measured along (a) $\overline{\Gamma H}$ axis and (b) the $\overline{\Gamma N}$ axis.

On both spectra, the peaks are QWSs corresponding to different quantum numbers (see Chapter 1).

An important step towards the understanding of electronic and magnetic properties of thin metal films is the measurement of the Fermi surface. The Fermi surface is the surface in momentum space that separates occupied from unoccupied states. The response of a metal to an electric, magnetic or thermal gradient depends on the shape of the Fermi surface, such properties depends on changes in the occupancy of states near the Fermi energy. The description of acquisition of the Fermi surfaces, by means of ARPES, is described in Chapter 2. Here we report constant energy cuts extracted from the Fermi surface maps. Fig. 4.12 shows the measured constant energy cut of the Fermi surface of 10 ML of Fe on W(110) with UP and DOWN magnetization. In the same figure the magnetization directions, the Brillouin zone and the high symmetry points are indicated.

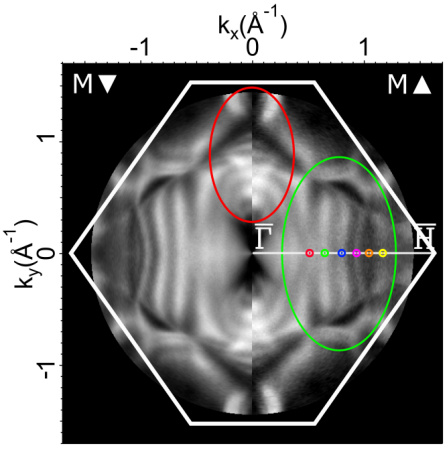

Figure 4.12: Constant energy cut of the Fermi surface measured on 10 ML of Fe/W(110) after magnetizing the film (left half) DOWN and (right half) UP. The maps were measured at constant BE=30 meV and using 55 eV photon energy.

In order to understand the nature of the different states visualized in the map of Fig. 4.12 we compare the measured map with the calculated Fermi surfaces of Fe and W projected on the (110) surface [42](see Fig. 4.13).

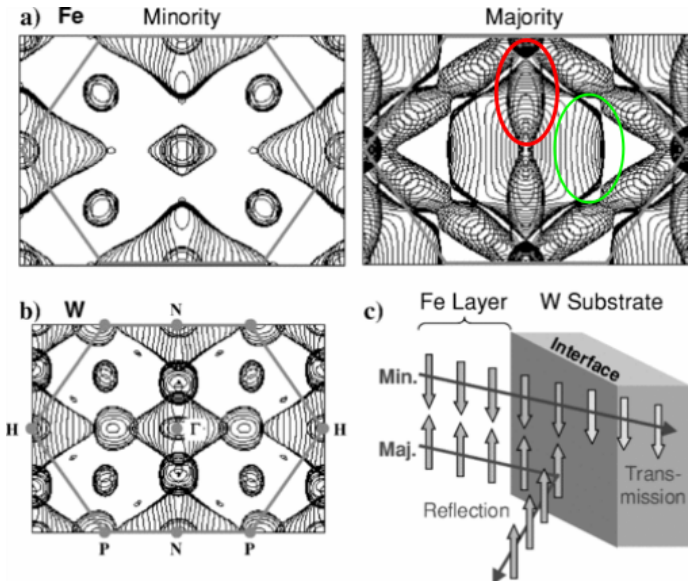

Figure 4.13: (a) Calculated spin-resolved (minority and majority) Fermi surface projected onto the (110) surface for (a) Fe and (b) W. (c) schematic representation of spin-polarized transmission at the Fe/W(110) interface [42].

In the measured map (Fig. 4.12), two different sets of electronic states are grouped with green and red ovals. By comparing the measured data (Fig. 4.12) with the calculated maps (Fig. 4.13), both groups of states have majority spin character. This behaviour may find explanation in the fact that, as predicted by the theory [42], the character of the states which exert confinement effects at the barrier with W is that of majority spin states (see Fig. 4.13 (c)), while minority states are resonant with the states of W (see Fig. 4.13 (b)) and should not give rise to QWSs.

To further study the impact of ferromagnetic-paramagnetic interface we examined the electronic structure of Fe films on another HM metal such as Mo(110). Fig. 4.14 reports the 2D intensity maps measured along the $\overline{\Gamma H}$ (k_x axis in Fig. 4.9) and $\overline{\Gamma N}$ (k_y axis in Fig. 4.9) of 10 ML of Fe on Mo(110). The measurements with negative values of k_x correspond to the magnetization of Fe "UP" while those with positive k_x correspond to the magnetization "DOWN". The sample was then rotated by 90° and the measurements were done along the $\overline{\Gamma N}$ direction (k_y in Fig. 4.9). Like in the case of Fe on W(110), QWSs are visible even if their energy separation is smaller than in the previous case.

Fig. 4.15 reports the MDC curves (Paragraph 4.1) extracted from the 2D photoemission intensity map of Fig. 4.14 (a) and (b) at BE= 30 meV. In Fig. 4.15 (a) there is the MDC spectrum along the $\overline{\Gamma H}$ direction (k_x axis), while in Fig. 4.11 (b) it is along the $\overline{\Gamma N}$ direction (k_y axis). The different QWSs are not clearly resolved like in the case of Fe on W(110) (see Fig. 4.11).

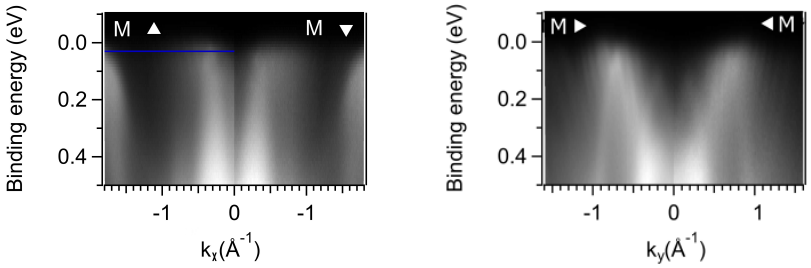

(a) (b)

Figure 4.14: 2D photoemission intensity maps measured on Fe film 10 ML thick deposited on Mo (110). The measurements were done (a) along the $\overline{\Gamma H}$ direction (k_x axis) and with the magnetization perpendicular to the scattering plane and (b) along the $\overline{\Gamma N}$ direction (k_y axis) with the magnetization in the scattering plane of the experiment. The photoemission maps were measured using 55 eV photon energy.

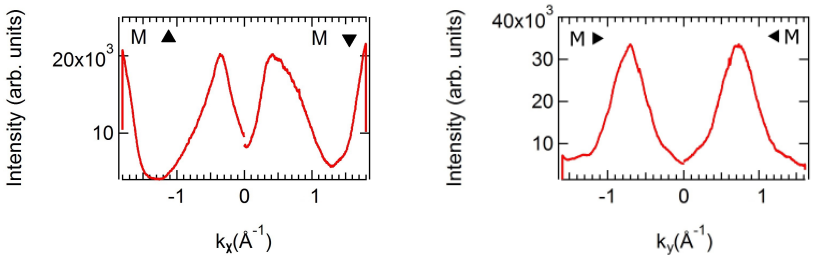

(a) (b)

Figure 4.15: MDCs extracted, at BE=30 meV, from the 2D intensity maps of Fig. 4.14. The MDCs cuts are measured along (a) the $\overline{\Gamma H}$ direction and (b) the $\overline{\Gamma N}$ direction.

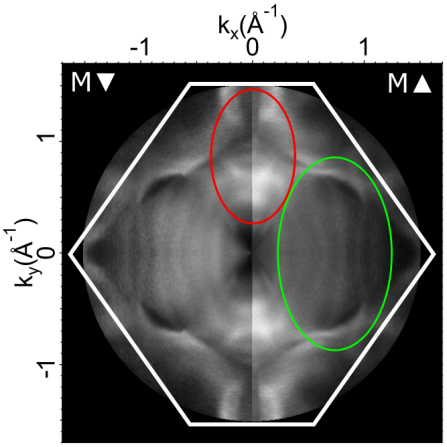

Figure 4.16: Constant energy cuts of the Fermi surface of 10 ML of Fe on Mo(110) with UP (right half) and DOWN (left half) magnetization. In the same figure the magnetization directions, the Brillouin zone and the high symmetry points are indicated. The spectra were measured using 55eV photon energy at 30 meV BE.

Fig. 4.16 shows the measured constant energy cut of the Fermi surface

of 10 ML of Fe on Mo(110) with UP and DOWN magnetization. In the same figure the magnetization directions, the Brillouin zone and the high symmetry points are indicated. Like in the case of Fe on W(110), we focus on two groups of electronic states. Similarly to the case of Fe on W we observe two families of states marked by green and red ovals (Fig. 4.12). Again the same effects of electron hybridization with the substrate prevent the observation of QWSs of spin-down character. The dispersion along the $\overline{\Gamma H}$ direction is more symmetric than for the Fe/W case, in close analogy with the electronic behaviour observed for the Co/W and Co/Mo interfaces.

5 Conclusions

In conclusion, we demonstrated that Yb grown on Mo(110) at RT forms atomically uniform films supporting QWSs. The homogeneous film thickness is obtained on the atomic scale within the region probed by ARPES measurements. The film thickness has been determined by comparing the measured and predicted [38] energy of the QWSs. The coverage of the investigated Yb films is in the range of 9 ML – 32 ML. Two groups of QWSs features find correspondence with the calculated band structure previously done for Yb(111) [39]. The electronic features detected close to E_F are not predicted by the calculation and their possible origin can be do to a small structural variation during the Yb film growth as already observed in the case of Yb film on W(110) [39].

In the case of Fe on HM we demonstrated that Fe films on W(110) and Mo(110) surfaces support QWSs. In the present experimental condition, the Fe QWSs visible on both substrates have mainly majority spin character, as clearly demonstrated by comparison with calculations of [42]. Fe spin down states, instead, are strongly coupled with corresponding states in the substrate and do not give rise to QWSs. The experimental results here obtained for Fe film of 10 ML thickness on W(110) and Mo(110) are the base for further ARPES measurements that will be dedicated to systematically study the electronic structure of Fe films on W and Mo as a function of different thicknesses. As mentioned in the Introduction, in this manner QWSs will be used as a tool for investigating buried interfaces and the obtained results can be used to improve also theoretical model predicting the electronic and magnetic structure at these interfaces.

By depositing Gd on W(110) at low temperature (T=84 K) and annaling it at T=795 K we observed a faint LEED pattern, but not QWSs. For this heterostructure, there is a hint that ordered film may be obtained using a two-step growth, but further investigation is necessary.

Bibliography

[1] C. Chappert, A. Fert, F. NguyenVan Dau, Nat. Mater. **6**, 813 (2007).

[2] K. Moser *et al.*, J. Phys. D **35**, R157 (2002).

[3] S. Batra, J. D. Hannay, H. Zhou and J. S. Goldberg, IEEE Trans. Magn. **40**, 319 (2004).

[4] H. Ohno *et al.*, Nature **408**, 944 (2000).

[5] D. Chiba *et al.*, Nature **455**, 515 (2008).

[6] E. B. Myers, D. C. Ralph, J. A. Katine, R. N. Louie and R. A. Buhrman, Science **285**, 867 (1999).

[7] D. C. Ralph and M. D. Stiles, J. Magn. Mater. **320**, 1190 (2008).

[8] A. Chernyshov *et al.*, Nat. Phys. **5**, 656 (2009).

[9] S. Ikeda, J. Hayakawa, Y. M. Lee, F. Matsukura, Y. Ohno, T. Hanyu, and H. Ohno, IEEE Trans. Electron Devices **54**, 991 (2007).

[10] I. M. Miron *et al.*, Nature **476**, 189 (2011).

[11] L. Liu *et al.*, Science **336**, 555 (2012).

[12] M. K. Brinkley, Y. Liu, N. J. Speer, T. Miller, and T.-C. Chiang, Phys. Rev. Lett. **103**, 246801 (2009).

[13] P. Moras, D. Wortmann, G. Bihlmayer, L. Ferrari, G. Alejandro, P. H. Zhou, D. Topwal, P. M. Sheverdyaeva, S. Blugel, and C. Carbone, Phys. Rev. B **82**, 155427 (2010).

[14] Masaru Kuno, *Introductory Nanoscience, Physical and chemical concepts* (Garland Science, Taylor&Francis Group, LLC, 2012).

[15] T.-C. Chiang, Surf. Sci. Rep. **39**, 181 (2000).

[16] I. Matsuda, T. Tanikawa, S. Hasegawa, H. W. Yeom, K. Tono and T. Ohta, Surf. Sci. Nanotech. **2**, 169 (2004).

[17] P. Moras, G. Bihlmayer. P.M. Sheverdyaeva, S.K. Mahatha, M. Papagno, J. Sanchez-Barriga, O. Rader, L. Novinec, S. Gardonio, and C. Carbone, Phys. Rev. B **91**, 195410 (2015).

[18] J. J. Paggel, T. Miller, and T.-C. Chiang, Phys. Rev. B **61**, 1804 (2000).

[19] K. Oura, V.G. Lifshits, A.A. Saranin, A.V. Zotov, *Surface Science, An Introduction* (Springer-Verlag, Berlin Heiderberg, 2010).

[20] L. Novinec, Bachelor thesis, Univerza v Novi Gorici, 2013.

[21] O. Rader and A. M. Shikin, Phys. Rev. B **64**, 201406 (2001).

[22] E. Bucher *et al.*, Phys. Rev. B **2**, 3911 (1970).

[23] E. Weschke, A. Yu. Grigoriev, C. Schüßler-Langeheine, Chandan Mazumdar, R. Meier, S. Vandré, S. Ram, L. Kilian, and G. Kaindl, C. Sutter , Phy. Rev. Lett. **83**, 584 (1999).

[24] http://www.elettra.trieste.it/lightsources/elettra/elettra-beamlines/vuv/vuvdescription

[25] http://www.elettra.trieste.it/lightsources/elettra/elettra-beamlines/badelph/description

[26] J. Malzbender, M. Przybylski, J. Giergiel, J. Kirschner, Surf. Sci. **414**, 187 (1998).

[27] https://vuo.elettra.eu/services/elements/WebElements.html

[28] S. A. Chambers and V. A. Loebs, J. Vac. Sci. Technol. A **10**, 1940 (1992).

[29] https://www.nist.gov/srd/nist-standard-reference-database-71

[30] A. Stenborg and E. Bauer, Phys. Rev. B **36**, 11 (1986).

[31] N. Martensson, A. Stenborg, O. Bjorneholm, A. Nilsson, and J. N. Andersen, Phys. Rev. Lett. **70**, 1731 (1988).

[32] E. D. Tober and R. X. Ynzunza, C. Westphal, C. S. Fadley, Phys. Rev. B **53**, 5444 (1996).

[33] D. Weller, S. F. Alvarado, W. Gudat, K. Schroder, and M. Campagna, Phys. Rev. Lett. **54**, 1555 (1985).

[34] Iwao Matsuda, Han Woong Yeom, Takehiro Tanikawa, Kensuke Tono, Tadaaki Nagao, Shuji Hasegawa, and Toshiaki Ohta, Phys. Rev. B **63**, 125325 (2001).

[35] J. Kolaczkiewicz and E. Bauer, Surf. Sci. **175**, 487 (1986).

[36] Ch. Roth, F.U. Hillebreeht, H.B. Rose, and E. Kisker, Phys. Rev. Lett. **70**, 3479 (1993).

[37] D. Wegner, A. Bauer, and G. Kaindl, Phys. Rev. Lett. **94**, 126804 (2005).

[38] M. I. Trioni *et al.* (unpublished).

[39] M. Bodenbach, A. Bohr, C. Laubschat, and G. Kaindl, M. Methfessel, Phys. Rev. B **50**, 14446 (1994).

[40] Inder P. Batra, S. Ciraci, G. P. Srivastava, J. S. Nelson, C.Y. Fong, Phys. Rev. B **34**, 8246 (1986).

[41] I. G. Baek, H. G. Lee, H.-J. Kim, and E. Vescovo, Phys. Rev. B **67**, 075401 (2003).

[42] J. Schafer, M. Hoinkis, E. Rotenberg, P. Blaha and R. Claessen, Phys. Rev. B **75**, 092401 (2007).

[43] S. Datta and B. Das, Appl. Phys. Lett. **56**, 665 (1990).

[44] J. Carlos Egues, Guido Burkard and Daniel Loss, Appl. Phys. Lett. **82**, 2658 (2003).

[45] M. Tsoi, A. G. M. Jansen, J. Bass, W. C. Chiang, M. Seck, V. Tsoi, and P. Wyder, Phys. Rev. Lett. **80**, 4281 (1998).

[46] J. Z. Sun, J. Magn. Magn. Mater. **202**, 157 (1999).

[47] J. A. Katine, F. J. Albert, R. A. Buhrman, E. B. Myers, D. C. Ralph, Phys. Rev. Lett. **84**, 3149 (2000).

[48] O. Fruchart, P. O. Jubert, M. Eleoui, F. Cheynis, B. Borca, P. David, V. Santonacci, A. Li´enard, M. Hasegawa and C. Meyer, J. Phys. Condens. Matter **19**, 053001 (2007)